Material Performance Determination for Nozzle Erosion in Hybrid Rocket Motors

by

Büşra Kahraman

A Dissertation Submitted to the
Graduate School of Sciences and Engineering
in Partial Fulfillment of the Requirements for
the Degree of

Master of Science

in

Mechanical Engineering

January 2023

Material Performance Determination for Nozzle Erosion in Hybrid Rocket Motors

Koç University

Graduate School of Sciences and Engineering

This is to certify that I have examined this copy of a master's thesis by

Büşra Kahraman

and have found that it is complete and satisfactory in all respects,
and that any and all revisions required by the final
examining committee have been made.

Committee Members:

_____

Assoc. Prof. M. Arif KARABEYOĞLU (Advisor)

_____

Prof. Dr. Metin MURADOĞLU

_____

Prof. Dr. Tahsin Çağrı ŞİŞMAN

_____

Prof. Dr. Onur TUNÇER

Date: 10.01.2023

‘To my family’

ABSTRACT

Material Performance Determination for Nozzle Erosion in Hybrid Rocket Motors

Büşra Kahraman

Master of Science in Mechanical Engineering

January 2023

Performance parameters such as thrust coefficient (C_F) and specific impulse (I_{sp}) are critical for rocket motor design. An increase in the nozzle throat area causes a change in C_F, thrust, and I_{sp}. Therefore, no erosion or minimal erosion is expected. Nozzle erosion in hybrid rocket motors is a prominent factor that should be studied since hybrid rocket motors (HRM) are still developing.

This study investigates the erosion rates of different materials at various oxidizer-to-fuel ratios (O/F), equivalence ratios, and chamber pressures. Moreover, the effects of throat length on erosion were investigated as well.

Performances of different graphite grades, metals, composites, and silicon carbide as nozzle materials were determined. The silicon carbide sintering procedure and the use of silicon carbide in hybrid rocket motors as nozzle material is one of the most important parts of this study due to being a research topic all by itself. There is only a few research on the use of SiC nozzles in HRM nozzles.

Static firing test results are given, and erosion rates of nozzle throats are measured for each test. Nozzle throat diameters are measured before and after the tests using both calipers and image processing toolbox in MATLAB®.

Results show that material selection and reduced O/F ratios are the most critical factors for lower erosion rates. Fine graphite grades may be good options for rocket nozzles, but silicon carbide is a promising material due to its high strength.

ÖZETÇE

Hibrit Roket Motorlarında Lüle Erozyonu için Malzeme Performansının Belirlenmesi

Büşra Kahraman

Makine Mühendisliği Yüksek Lisans

Ocak 2023

İtki katsayısı (C_F) ve özgül itki (I_{sp}) gibi motor parametreleri, roket motor tasarımı için kritik öneme sahiptir. Lüle boğaz alanındaki artış, itki katsayısı ve özgül itkide değişikliğe sebep olur. Bu nedenle, erozyonun hiç olmaması ya da minimum seviyede olması beklenir. Hibrit roket motorlarında lüle erozyonu, hibrit roket motorları hala gelişmekte olduğundan, üzerinde çalışılması gereken önemli bir faktördür.

Bu çalışma farklı malzemelerin, çeşitli oksitleyici-yakıt oranlarında ve yanma odası basınçlarında, aşınma oranlarını araştırmaktadır. Ayrıca lüle boğaz uzunluğunun erozyona etkisi de incelenmiştir. Lüle malzemeleri olarak farklı grafit tipleri, metaller, kompozitler ve silisyum karbürün performansları belirlenmiştir. Silisyum karbür sinterleme işlemi ve silisyum karbürün hibrit roket motorlarında lüle malzemesi olarak kullanılması başlı başına bir araştırma konusu olması nedeniyle bu çalışmanın en önemli kısımlarından birisidir. Hibrit roket motorlarında silisyum karbür lülelerin kullanımı ile ilgili sadece birkaç araştırma bulunmaktadır.

Statik ateşleme testi sonuçları verilmiş ve her test için lüle boğazının aşınma oranları ölçülmüştür. Lüle boğaz çapları, testlerden önce ve sonra MATLAB®'deki görüntü işleme araç kutusu ve kumpas kullanılarak ölçülmüştür.

Test sonuçları, malzeme seçiminin ve azaltılmış oksitleyici-yakıt oranlarının, daha düşük erozyon oranları için en önemli faktörler olduğunu göstermektedir. İyi grafit çeşitleri, roket lüleleri için iyi birer seçenek olabilir, ancak silisyum karbür, yüksek mukavemetinden dolayı umut vadeden bir malzemedir.

ACKNOWLEDGMENTS

I would like to present my gratitude and special thanks to my advisor, Assoc. Prof. Mustafa Arif Karabeyoğlu for his support throughout my study and his motivation, encouragement, and guidance. I always admire his thoughts and knowledge. It is a privilege to work with him.

I would like to express my most profound appreciation to Prof. Dr. Tahsin Çağrı Şişman for his immense encouragement during my undergraduate study. I also thank him for preparing me for this master's research and for his advice.

I would also thank my thesis defense juries Prof. Dr. Onur Tunçer and Prof. Dr. Metin Muradoğlu, for their precious comments and for reviewing my thesis.

I would like to express my special thanks to my colleague Dr. Mustafa Baysal. His willingness to share his knowledge is priceless. His contributions to me and this study are inestimable to me. He always encouraged me to do graduate study. I am fortunate to have had a chance to meet and work with him.

I am also very thankful to my colleague Dr. Hakkı Karakaş for his support and contributions. He inspired me when I started the job and shared his knowledge. I look forward to writing articles and doing firing tests together again.

I also thank my colleagues Utku Can Yıldız, Nur Ber Emerce, and Uğur Kokal for their friendship, help, advice, and brilliant ideas. I am also grateful to Serhan Enes Kalmış, Yiğit Hamza Yıldız, and Barış Emre Kıral for their support and contribution to this study.

I am also very thankful to Murat Çetinkaya for making me feel like he is always by my side and for his help during this research.

Furthermore, I would like to thank DeltaV Space Technologies Inc. for the opportunities they provide, such as using test facilities, material supply, and manufacturing. I am very grateful to DeltaV Space Technologies Inc. for allowing me to do my master's degree. Besides, I am very thankful to DeltaV technicians, especially to Tarık Tiryaki, Semih Çalışkan, Cengiz Uygun, and Erkan Solmaz for their help and sacrifices during manufacturing processes and firing tests.

I am also thankful to Bilal Çakar and his company 'Bileşke Makine & Mühendislik' for his help with material supply and sacrifices during manufacturing processes.

Finally, I would like to give my deepest gratitude to my mother, Hülya Kahraman; my father, Tuncer Kahraman; my sister Tuğçe Kaçır, my brother-in-law Cengizhan Kaçır, and my nephew Ömer Aras Kaçır for their unconditional love and endless support.

TABLE OF CONTENTS

LIST OF TABLES

LIST OF FIGURES

NOMENCLATURE

a	Regression Rate Coefficient
A	Area
C_d	Discharge Coefficient
c*	Characteristic Velocity
C_F	Thrust Coefficient
D	Diameter
D	Diffusivity
F	F Force
g_0	g_0 the Standard Acceleration due to Gravity
G	G Local Mass Flux
I_{sp}	I_{sp} Specific Impulse
k	k Specific Heat Ratio (Gamma)
M	M Mass
MW	MW Molecular Weight
$\dot{m}$	$\dot{m}$ Mass Flow Rate
P	P Pressure
$\dot{r}$	$\dot{r}$ Regression Rate
$\dot{r}_n$	$\dot{r}_n$ Erosion Rate
Re	the Reynold's Number
Sc_i	the Schmidt Number
T*	Dimensionless Temperature
T	Thrust
V	Velocity
η	Efficiency
Ω	The Dimensionless Collision Integral
Δ	Boundary Layer Thickness
ξ	the Stoichiometric Mass Ratio
σ	Distance Parameter

Supercripts

n	Mass Flux Exponent

Subscripts

e	Exit
f	Final
i	Initial
n	Nozzle
net	Net
o	Oxidizer
ox	Oxidizer
p	Port
p	Propellant
ref	Reference
s	Surface
t	Throat
theo	Theoretical
0	Initial

Abbreviations

HRM	Hybrid Rocket Motor
HDPE	High Density Polyethylene
HTPB	Hidroxyl Termianated Polybutadiene
LOX	Liquid Oxygene
LRE	Liquid Rocket Engines
L/D	Length to Diameter Ratio
O/F	Oxidizer to Fuel Ratio
SiC	Silicon Carbide
SRM	Solid Rocket Motors

Chapter 1:
INTRODUCTION

1.1 History and Working Principles of Rockets

Rockets have been the subject of human curiosity for centuries. Rockets are the only way of reaching and discovering space. Therefore, humans have always sought to reach space cost-effectively. Hero of Alexandria, who lived between 10-85 AD, invented a steam engine, and the working principle of this engine was the same as rocket propulsion systems. He used two L-type pipes and one sphere in his machine. Obtained torque by using the steam which goes through the L pipes [1]. For centuries importance of this machine was not understood. By 1232, China had developed fire arrows to repel invaders. These fire arrows consist of bamboo tubes that have gunpowder in them. It is accepted that the birth of rockets started with fire arrows. It is believed that modern rocket science started with Konstantin Tsiolkovsky in the 19th century [2]. He was a mathematics teacher and had many ideas about rockets and satellites. He published many articles about rockets and astronomy. He derived a rocket equation (Equations 1.4&1.5) that is called as 'Tsiolkovsky Rocket Equation' and describes the motion of a rocket [3] [4]. Furthermore, this equation is still used for rocket calculations. In Figure 1.1, there is an illustration of Tsiolkovsky's rocket design [3].

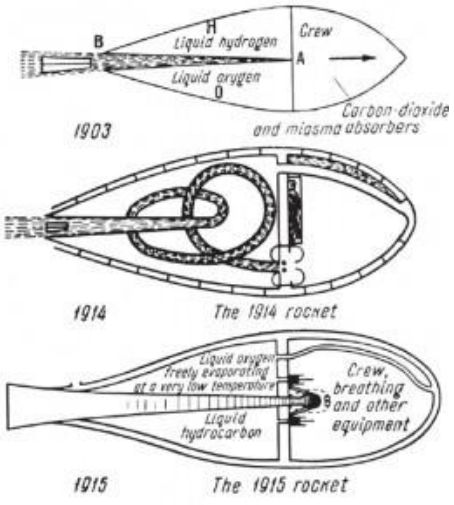

Figure 1.1: An illustration of Tsiolkovksy's rocket design *[3]*

In 1923, German physicist Hermann Oberth published his dissertation about rocket propulsion and space travel, but his dissertation was rejected because it was very speculative for these years. He designed a liquid rocket engine for space travel that used liquid oxygen and alcohol as oxidizers and fuels. His liquid-engine rocket design can be seen in Figure 1.2 [5].

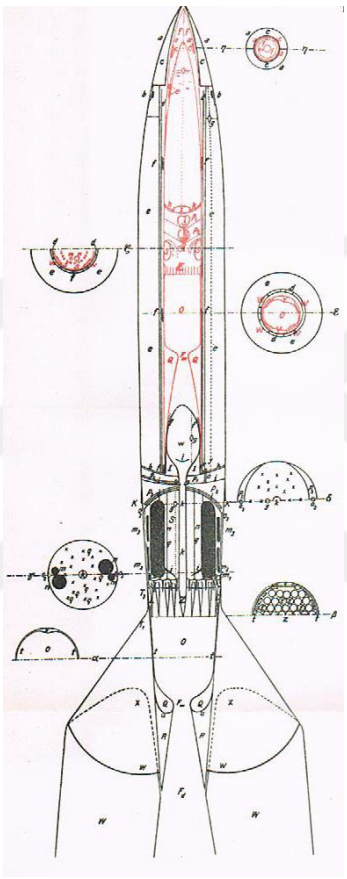

Figure 1.2: Hermann Oberth Rocket Design *[5]*

Another founding father of rocketry, American physicist Robert Goddard published a book named ‘A Method of Reaching Extreme Altitudes’ in 1919 and had two patents about liquid fuel and staged rockets. Moreover, he built the world’s first-liquid engine rocket and flew it in 1926. Even if the rocket did not reach extreme altitudes, his ideas underpinned the birth of the Saturn V rocket [2] [6]. Wernher von Braun was influenced by Hermann Oberth and developed the V2 rocket (Figure 1.3), which Germany used in World War 2 [7].

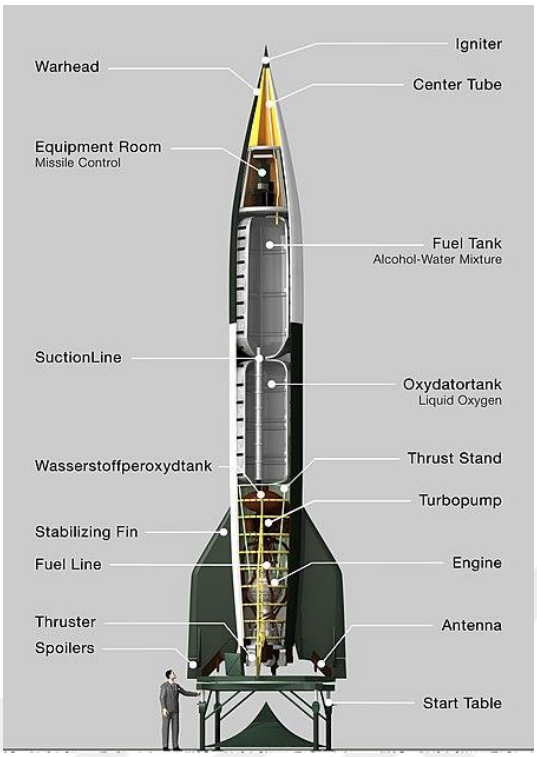

Figure 1.3: V2 Rocket Illustration *[7]*

During the same years, Russian scientist Sergei Korolev, the man responsible for the first human spaceflight, was developing missiles for Russia. He started to design launch vehicles to compete with the American Saturn V rocket and developed the N-1 rocket (Figure 1.4) [8].

Figure 1.4: The N-1 Booster *[8]*

The working principle of rockets is based on Newton's 2nd and 3rd Law (Equation 1.1). The propellant is ejected from the rocket nozzle as the rocket nozzle applies a force on the propellant. According to the 3rd law, the propellant applies an equal but opposite direction force on the rocket. Hence, Newton's 2nd Law can be written as in Equation 1.2, named 'momentum thrust.' Thrust is not only related to the change in momentum but also related to the atmospheric and local pressures. If the rocket is considered a control volume, the effect of gas pressure changes should be added to the thrust equation. Since most rockets have fixed nozzle throat areas, there is only one optimum altitude level for the rockets. The exit and ambient pressure are imbalanced due to altitude change. Therefore, a 'pressure thrust' term should be added to Equation 1.2 (Equation 1.3) [9].

$$F_{net} = M\frac{dV}{dt} \tag{1.1}$$

Where F_{net} is the net force, M is the mass of the rocket, and $\frac{dV}{dt}$ is the velocity change of the rocket.

$$T = \dot{m}V_e \tag{1.2}$$

Where T is thrust, $\dot{m}$ is the propellant mass flow rate, and V_e is the exit velocity.

$$F = \dot{m}V_e + (p_e - p_a)A_e \tag{1.3}$$

Where p_e is exit pressure, p_a is ambient pressure, and A_e is the exit area of the nozzle. In this situation, the pressure term is zero when the atmospheric pressure equals the exit pressure. In a vacuum environment, ambient pressure is zero, and the pressure term consists of only the exit pressure and exit area. Pressures are not the only thing that changes during the combustion, the amount of fuel in rockets also varies. Tsiolkovsky derived his equation by considering this issue, and his equation can be defined as;

$$\Delta V = V_e ln\left(\frac{M_0}{M_f}\right) \tag{1.4}$$

Where ΔV is the change in the velocity of the rocket, V_e is the exit velocity, M_0 is the initial mass of the rocket, and M_f is the final mass of the rocket. Exit velocity can be written in terms of specific impulse I_{sp} and the standard acceleration due to gravity g_0, which is 9.81 m/s^2. Therefore, Equation 1.4 can be rewritten as;

$$\Delta V = I_{sp} g_0 ln\left(\frac{M_0}{M_f}\right) \tag{1.5}$$

ΔV is an essential parameter for rockets. For example, if a system requires high ΔV, system performance parameters, such as I_{sp} and mass ratio, are critical. Not only I_{sp} is important, but also nozzle area ratio is important. If a rocket nozzle area ratio changes, exit velocity changes as well. As a result of a shift in exit velocity, ΔV also changes. In reference [10], Narsai expressed that if the nozzle area ratio decreases to 26.8 from 200, the rocket designed needs an additional 900 kg of propellant to meet the required ΔV of the system. Therefore, the nozzle area ratio is a critical parameter for rockets.

The propulsion systems of the rockets are separated mainly into four parts: Electric, nuclear, chemical, and cold gas (Figure 1.5). Most rockets use chemical propulsion systems due to their advantages during lift-off. Electrical propulsion systems use electrical power to accelerate, and their thrust levels are less than the chemical propulsion systems. Therefore, electrical propulsion systems are commonly used for in-space thrusters. Chemical propulsion systems are separated into three parts: Liquid propulsion systems, solid propulsion systems, and hybrid propulsion systems. Liquid rocket engines are generally preferred for launch vehicles due to their high I_{sp} performance. In liquid rocket engines, oxidizers and fuels are stored in separate tanks and transmitted in the combustion chamber using valves. Liquid propellant rocket engines have advantages such as high I_{sp}, restart capability, and throttling, but their complexity is a shortcoming.

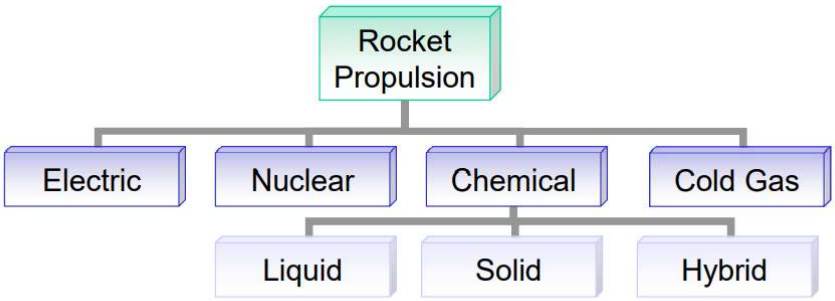

Figure 1.5: Rocket Propulsion Systems *[11]*

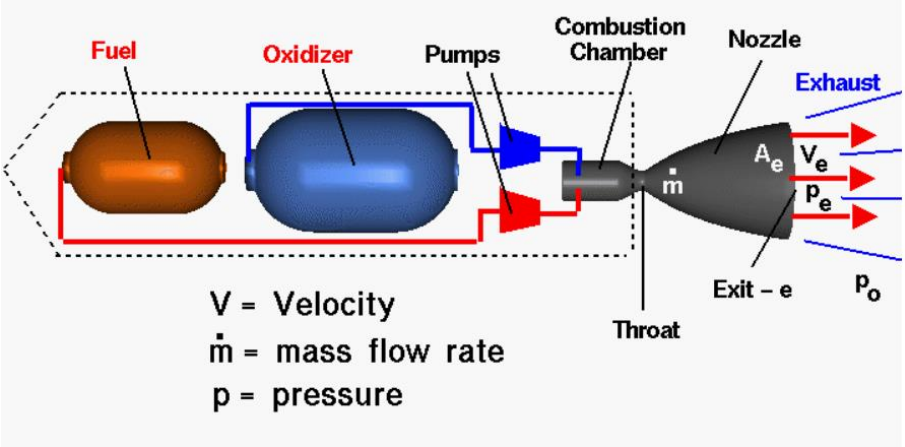

Figure 1.6: Schematic of Liquid Propellant Rocket Engine *[12]*

Another crucial chemical propulsion system is solid propellant motors. They have fuels and oxidizers in the solid phase. Since fuel and oxidizer are stored together, solid rocket motors are hazardous and have a chance to explode. Although their disadvantages, they have some advantages. For example, they are used in missiles and boosters of launch vehicles due to their high density, easy firing, and less complexity. In Figure 1.6, there is a schematic of a solid rocket motor.

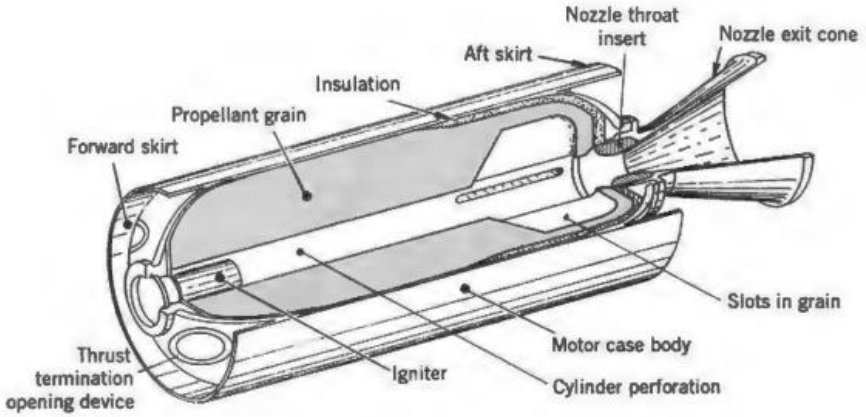

Figure 1.7:Solid Propellant Rocket Motor *[9]*

1.2 Hybrid Rocket Propulsion Fundamentals

Unlike solid rocket motors, fuel and oxidizer are stored in separate regions in hybrid rocket motors. Usually, the oxidizers are in liquid or gas form, and the fuels are in solid form. In general, HRMs generate thrust by burning liquid oxidizers and solid fuels. [13]

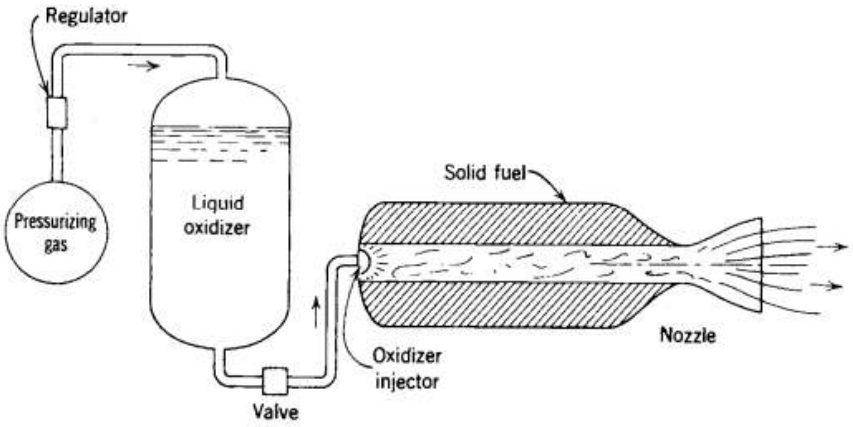

Figure 1.8: Hybrid Rocket Motor Design *[9]*

Hybrid rockets have many advantages compared with solid rocket motors. HRMs give higher theoretical Isp than SRMs. In addition, they have fewer explosion hazards due to the separation of oxidizer and fuel. For this reason, they are easy to handle during transporting and assembly. HRMs have restart capability and throttling, so they are more controllable than SRMs.

HRMs have some advantages compared with liquid rocket engines as well. HRMs mechanically simpler than the LREs, because they only need less plumbing and valves. Moreover, turbopumps used in LREs to pressurize the oxidizer are very complex, but in HRMs, self-pressurized oxidizers can be used, or work with a blow-down system. Since the fuel of HRM is in the solid phase, it is denser than liquid fuel. Therefore, the fuel of HRM decreases the volume of the entire system. This means that the system is more minor, and the operations with the smaller system are easier. Furthermore, their significant advantages are hybrid rocket motors' reduced development and management costs [13].

HTPB, HDPE, Plexiglas, polyethylene, nylon, and waxes are used as solid fuels in HRMs. Usually, liquid oxygen, gaseous oxygen, nitrous oxide, hydrogen peroxide, nitric acid, and nytrox are the oxidizers used in HRMs. [14] Since LOX is a cryogenic oxidizer, it takes work to handle. HRMs have a significant shortcoming: low regression rate even if they have many advantages. Liquefying theory of paraffin-based fuels gives higher regression rates at similar mass fluxes [13] [15].

In hybrid rocket propulsion systems, the oxidizer is injected into a port in the solid fuel grain, and the fuel grain melts under the flame. For this reason, a liquid layer forms

on the burning surface of the solid fuel. High gas velocities in the port cause liquid layer instabilities, so droplet formation occurs, and mass transfer results in the entrainment of liquid droplets from the melt layer (Figure 1.8) [15] [16]. These liquefying propellants increase the regression rate. A considerable amount of study in liquid layer hybrid combustion theory can be seen in Ref. [15]. The regression rate of a hybrid rocket motor can be calculated using Equation 1.6, where a is the regression rate coefficient, n is the mass flux exponent, and G is the local mass flux in the port [13] [17]

$$\dot{r} = aG^n x^m \tag{1.6}$$

Mass flux in the port can be defined as

$$G = \frac{\dot{m_{ox}}}{A_p} \tag{1.7}$$

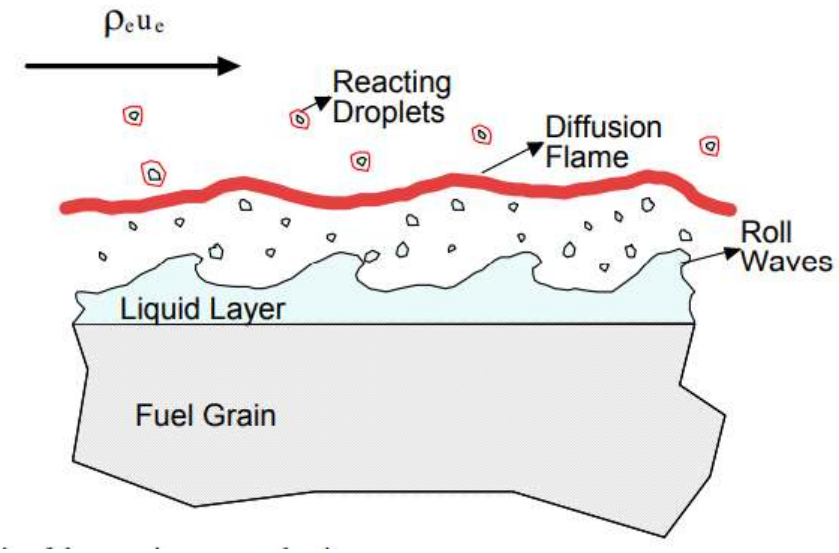

Figure 1.9: Schematic of Liquid Entrainment Mechanism *[16]*

Karabeyoğlu stated that paraffin waxes have the best properties among the n-alkanes due to their higher regression rates at relatively high temperatures [16]. In Reference [17], Karabeyoğlu assumed that the fuel is burning uniformly along the grain, and the effects of space-averaging are ignored for simplicity. Therefore, he derived three different mass flux equations based on the port diameter, port area, and mass flux. See Equation 1.8 for the mass flux equation based on the port diameter.

$$\bar{G}_{oD} = \frac{16\dot{m}_o}{\pi(D_i+D_f)^2} \tag{1.8}$$

D_i is the initial port diameter, D_f is the final port diameter, and $\dot{m}_o$ is the oxidizer mass flow rate.

Equation 1.9 for the mass flux equation that based on the port area.

$$\bar{G}_{oA} = \frac{2\dot{m}_o}{A_{pi}+A_{pf}} \tag{1.9}$$

Where A_{pi} is the initial port area and A_{pf} is the final port area.

Equation 1.10 for the mass flux equation that based on the mass flux

$$\bar{G}_{oF} = 0.5\left(\frac{\dot{m}_o}{A_{pi}} + \frac{\dot{m}_o}{A_{pf}}\right) \tag{1.10}$$

1.2.1 Scope of This Study

In this study, gaseous oxygen is used as an oxidizer to see the nozzle erosion rates better since GOX erosion rates are higher than nitrous oxide because of the amount of oxidizing agents and higher combustion temperature. GOX is also easy to handle because it is not cryogenic and is not affected by temperature much. In addition, it does not require complex valves or need heating since it is at room temperature.

This study investigates the performances of different materials used for the nozzle. Materials are tested by using a small-scale hybrid rocket motor. Since a slight change in the nozzle area ratio causes a significant difference in motor performance in small systems, the material's durability is indispensable, especially in long-burning hybrid rocket motors.

Five different graphite grades, composite materials, tungsten, molybdenum, and silicon carbide were tested. Composite materials and silicon carbide were manufactured in DeltaV Space Technologies. Since graphite is the most common material used in hybrid and solid rocket motors, this study prioritizes different graphite grades. However, ceramics and ceramic matrix composites are also convenient for high temperatures, so the sintering procedure of silicon carbide is also one of the essential parts of this study. This study's contribution to the literature gives a strong idea about materials that can be used in hybrid rockets.

Chapter 2:
NOZZLE EROSION THEORY

2.1 Nozzle Erosion Literature Review

Nozzle erosion became an essential phenomenon in the middle of the 20th century. In Reference [18], Meyer et al. studied the oxidation behavior of carbon with different combustion products, such as O_2, CO_2, and H_2O. In addition to this study, Strickland studied the interaction between oxygen and carbon filaments at high temperatures in Reference [19]. In light of such information, nozzle erosion in rocket motors became even more critical, and research about this phenomenon increased day by day. Kamps [20] studied the chemical erosion in hybrid rocket motors using heterogeneous reactions, which are derived by Meyer et al. and Strickland [18] [19].

HRMs used in space applications are exposed to higher temperatures and heat transfer for a long time. This phenomenon causes oxidation and higher heat transfer to the nozzle material, leading to higher erosion rates. In general, there are two main approaches to solve erosion problems. In reference [21], it is stated that the regenerative cooling is the most appropriate method for steady-state approaches. On the other hand, ablative cooling is the most viable way for the transient systems. Regenerative cooling is usually used for the LREs, because their fuel and oxidizers are both in liquid phase. Given fuel in the pipes around the nozzle cools the nozzle and enters the combustion chamber with the help of the pipes. Despite the LREs, ablative cooling is preferred HRMs. In general, oxidizers of the HRMs are hazardous at high temperatures, therefore regenerative cooling is not feasible for the HRMs even though it is possible in theory. For this reasons, ablative materials have been preferred for HRM nozzles and widely used. Due to its wide availability, graphite nozzles are one of the most common materials in solid and hybrid rocket motor nozzles. Kamps separated the major categories that are used for the HRMs in terms of chamber pressure and size. See Figure 2.1 [20]. Since, ceramics and graphite are brittle, they cannot be suitable for high pressure applications. At high pressures, refractory metals can be preferred due to their strong mechanical properties. Even though pressures are high, refractory metals cannot be used for large scale motors due to their

high density, because the lightness is very important parameter for rockets. In these conditions, ceramic matrix composites can be preferred due to their lightness and resistivity to high temperatures. Kamps also investigated the graphite nozzle erosion rates at different equivalence ratios and chemical erosion mechanisms in hybrid rocket motors [22].

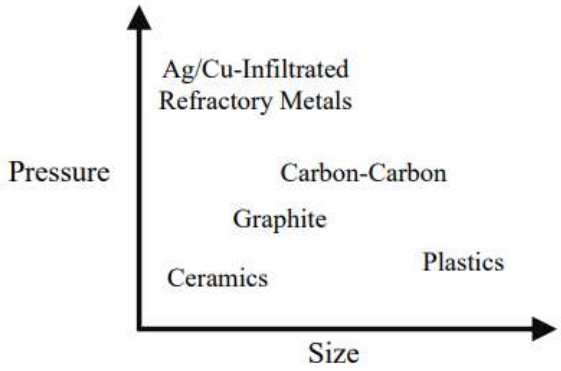

Figure 2.1: Material Selection for Nozzle Based on Pressure and Size *[20]*

Nozzle erosion may be separated into two main types: chemical and mechanical. It is known that the erosion in the HRM nozzles is caused by the oxidizing agents in the combustion products that react with the nozzle material unlike SRMs [13].

Nozzle erosion is a significant parameter since it affects the motor performance directly. For this reason, modeling of reaction between the nozzle material and combustion products are necessary for accurate calculations [23]. In reference [24], Bianchi & Nasuti obtained a thermochemical ablation model which considers the heterogeneous chemical reactions at nozzle surface which is used in this study as well.

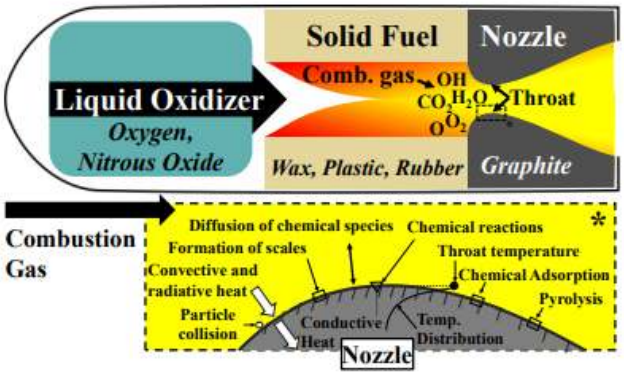

Figure 2.2: Erosion Mechanisms in HRMs *[22]*

In addition to the pure graphite research, Whitmore et al. studied to minimize nozzle erosion rates in long burning HRMs by using pyrolytic graphite and boron nitride. Whitmore et al. propounds that using the pyrolytic graphite & boron nitride as nozzle material gives a significant decrease in nozzle erosion rates compared to the similar test conditions which use pure graphite in nozzles [25]. In Figure 2.4, test results of reference [13] and [25] are compared.

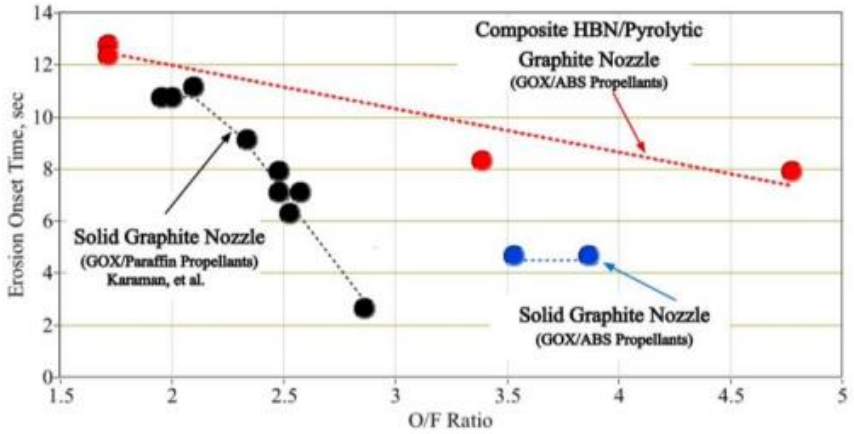

Figure 2.3: Erosion Onsets of HBN/Pyrolytic Graphite vs Solid Graphite *[25]*

Researchers have started to minimize nozzle erosion rates due to its effects on the performance of the rocket. Karakas et al. stated that the addition of micro aluminum to the paraffin-based fuel has a great effect on the erosion rates. Al_2O_3 formation occurs between the aluminum in the fuel and the oxidizer, so the amount of the oxidizing agents decreases. Therefore, due to the lack of free oxygen, chemical reactions between the nozzle material and the combustion products are diminished [26]. Moreover, metallic powders such as $LiAlH_4$, NBH_6, and Mg also cause a significant reduction in the nozzle erosion rates. Even though, $LiAlH_4$ and NBH_6 have a positive impact on the performance of the rocket motor, they are not preferred due to their high costs. Besides, their fuel preparation processes are not easy, and they can be hazardous [27] [28]. See Figure 2.5 to see the effect of metallic powders on the nozzle erosion rates. In these tests N_2O is used as oxidizer.

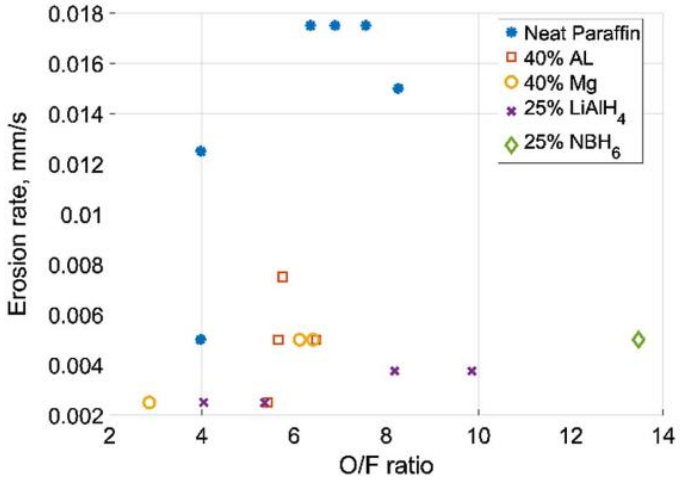

Figure 2.4: Effect of Metallic Powders on the Erosion Rates *[26]*

In conclusion, erosion is one of the most important parameters that effects the performance of the rocket motors. Therefore, researches continue to predict the nozzle erosions rates and techniques to minimize erosion rates are studied by the researchers.

2.2 Nozzle Design

Nozzles are generally separated into three parts: subsonic, sonic, and supersonic nozzles. Supersonic nozzles are used in rockets due to their high-pressure ratios. High pressure ratios are significant to obtain high energies. At the nozzle throat, the flow is sonic. Since the speed of sound is nearly equals to the speed of the pressure wave in the chamber, it is not possible for a disturbance to pass the sonic flow. Therefore, the flow is frozen, and does not know that the exit pressure is decreasing. This situation is called as choked flow and the flow is choked at the nozzle throat [29] [30]. In choked flow calculations, Equation 2.1 is used. Mass flow through the rocket is a function of throat area, chamber pressure, specific heat ratio of the combustion products, and the temperature.

$$\dot{m} = \frac{A_t + v_t}{V_t} = A_1 p_1 k \frac{\sqrt{[2/(k+1)]^{(k+1)/(k-1)}}}{\sqrt{kRT_1}} \tag{2.1}$$

Where p1 is the stagnation pressure, v_t is the velocity, and V is the specific volume.

For a supersonic nozzle, inverse nozzle area ratio can be expressed in terms of specific volume, velocity, pressure, and specific heat ratio. See Equation 2.2 [29]. In the equation ‘y’ reveals that the conditions at any downstream location. Nozzle area ratio can be calculated by using Equation 2.2.

$$\frac{A_t}{A_y} = \frac{V_t v_y}{V_y v_t} = \left(\frac{k+1}{2}\right)^{1/(k-1)} \left(\frac{p_y}{p_1}\right)^{1/k} \sqrt{\frac{k+1}{k-1}\left[1 - \left(\frac{p_y}{p_1}\right)^{(k-1)/k}\right]} \quad (2.2)$$

In this study, nozzle throat area is calculated by using the Equation 2.3 [31]

$$A_t = \frac{\dot{m}_p c^*_{theo} \eta_c}{C_d P_c} \quad (2.3)$$

Where $\dot{m}_p$ is the propellant mass flow rate, c^*_{theo} is the theoretical characteristic velocity, η_c is the combustion efficiency, C_d is the discharge coefficient, and P_c is the chamber pressure. Regression rate formula which is given in Equation 1.6 is used to calculate regression rates in the tests. By using the regression rate fuel mass flow rate is calculated. Average oxidizer mass flow rate is calculated by using the temperature and pressure data in the test line. Therefore, total propellant mass flow rate can be calculated by adding oxidizer mass flow rate to the fuel mass flow rate. c* is taken from CEA, chamber pressure was selected nearly 25 bar for the initial condition.

2.3 Nozzle Erosion Calculation

Reduction in nozzle area is a function of O/F, local mass flux, and the a_n constant which is dependent on the reference pressure, erosion rate, combustion efficiency, and the c*.

Nozzle erosion rate can be written in terms of these properties,

$$\dot{r}_{n} = a_n (O/F)\, G_n^m \quad (2.2)$$

Where local mass flux is,

$$G_n = \frac{\dot{m}_p}{A_n} \quad (2.3)$$

By using c* equation, local flux can be rewritten as,

$$G_n = \frac{P_c C_d}{c^*_{theo} \eta_c} \frac{A_{nt}}{A_n} \quad (2.4)$$

Combining Equation 2.2 and Equation 2.4, regression rate of nozzle throat [31] can be written as;

$$\dot{r}_n = a_n (O/F) \left(\frac{C_d}{c^*_{theo} \eta_c}\right)^m \left(\frac{A_{nt}}{A_n}\right)^m P_c^m \quad (2.5)$$

A_n coefficient is a prominent factor to predict the nozzle erosion rates for a specific materials. Each material has an a_n coefficient which can vary with O/F. Tests that have the same chamber pressures and different oxidizer to fuel ratios can be used for predicting the a_n constant by using Equation 2.5 [31]. Experimental data is taken as a

reference, and a_n coefficient is calculated by making a linear erosion assumption for the nozzle material. Kahraman et al. stated that once obtaining the a_n constant, erosion prediction for the next tests can be made using CEA [13]. a_n constant is not derived for the materials that used in this study. It requires much more tests for each material to obtain more accurate results.

$$(\dot{r}_n)_{ref} = \alpha_n \left(\frac{C_d}{c^* \eta}\right)^m P_{cref}^m \tag{2.6}$$

Nozzle erosion rates are calculated by using the Equation 2.7 after the tests and obtaining the final diameters of the nozzle throat. Reactions at the nozzle surface started at high temperatures, therefore, there is no erosion expected until that time. Erosion starting time is named as erosion onset time and it is an important parameter for the calculation of the erosion rates. When considered from this point of view, if the onset time enough for not to erode, there will be no erosion. Erosion onset time is subtracted from the burn time to find the time period that chemical reactions occur. In Figure 2.5, begining of the nozzle erosion (onset time) is shown. If the tank pressure remains the same and there is a decrease in the chamber pressure, if there is no other explanation for the decreasing chamber pressure, reason of the decrease in pressure is the nozzle erosion.

$$\bar{\dot{r}_n} = \frac{D_{t_f} - D_{t_i}}{2(t_{burn} - t_{erosion\ onset})} \tag{2.7}$$

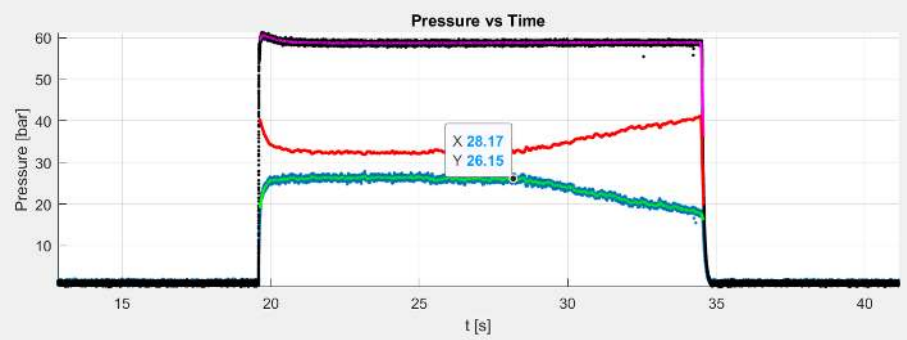

Figure 2.5: Erosion Onset Time

Initial and final throat diameters are measured by using t-scope and calipers. In addition to caliper measurement, an image processing MATLAB® code is used to calculate the final diameter of the throat. Manual calculations are compared with the image processing results and it is obvious that the results are very close to each other. In Reference [13], difference between the manual and image processing results were

expressed as nearly 2%. In Figure 2.6, example nozzle throat erosion photos that used in image processing are shown.

Figure 2.6:Grade 1 Erosion Photos Before and After the Test

2.4 *Effect of Nozzle Erosion on Rocket Performance*

The most prominent factor for the performance of a rocket is thrust. Thrust is a function of thrust coefficient C_F, throat area, and the chamber pressure. Thrust equation can be written as it is stated in Equation 2.8 [29]. C_F is a key parameter to analyze the performance of the rocket.

$$F = C_F A_t P_c \tag{2.8}$$

Equation 2.8 can be rewritten,

$$C_F = \frac{F}{A_t P_c} \tag{2.9}$$

By using isentropic relations C_F can be expressed in terms of the pressure ratio, area ratio, and specific heat ratio [29]. In Equation 2.10, it can be clearly seen that C_F is directly proportional to the throat area although it is a function of pressure ratio. Therefore, a slight change in nozzle throat area directly affects the C_F and the thrust as well. For γ=1.3, C_F curves are shown in Figure 2.7 for a nozzle at different area and pressure ratios. The black dashed line represents the optimum thrust coefficient for the case which the ambient pressure is equal to the exit pressure.

$$C_F = \sqrt{\frac{2k^2}{k-1}\left(\frac{2}{k+1}\right)^{(k+1)/(k-1)}\left[1-\left(\frac{p_e}{p_c}\right)^{(k-1)/k}\right]} + \frac{p_e - p_a}{p_c}\frac{A_e}{A_t} \tag{2.10}$$

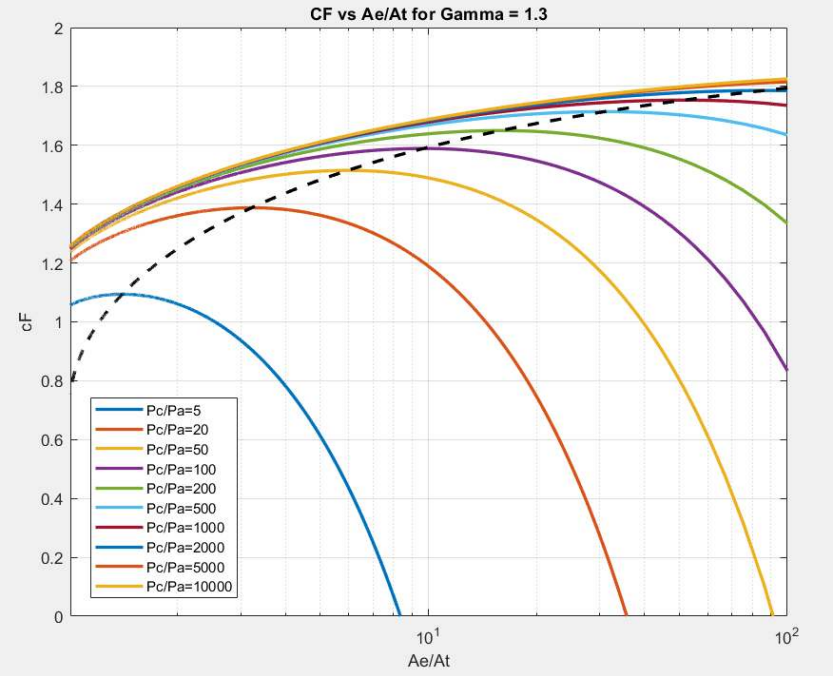

Figure 2.7: Thrust Coefficient vs Area Ratio Curves

The difference between the exit pressure at the nozzle exit and the ambient pressure affects the nozzle performance. If the rocket is designed for the space, it is expected to have an exit pressure equal to the ambient pressure which is zero, but if the rocket is operating in the atmosphere, there is not only one optimum condition for the nozzle. Since the ambient pressure changes with the altitude, nozzle should be designed for one condition that gives maximum thrust. As altitude changes, separation of the nozzle exit occurs due to the change in the ambient pressure. Separation generally occurs at if the ratio of the exit pressure and the ambient pressure is nearly 0.35- 0.4 in regard to the Summerfield criterion [32]. The flow expands through the nozzle extension but if the exit area is not enough to expand, the flow continues to expand at the outside of the nozzle extension. Under-expanded condition occurs when the exit area of the nozzle is too small to give the pressure equal to the atmospheric pressure. Most of the rockets fly with an under-expanded nozzle since there is only one optimum nozzle for each altitude. If the exit area is too large for the optimum condition, the flow at the exit has a pressure level that is lower than the ambient pressure. Unlike the under-expansion, over-expansion is cause a significant loss in C_F and I_{sp}. Even if there is a loss in under-expanded nozzles, over-expansion nozzles are more inefficient due to the shock waves and for higher ambient pressures flow separation starts in the nozzle extension. In Figure 2.8 under-expanded and over-expanded nozzles can be seen.

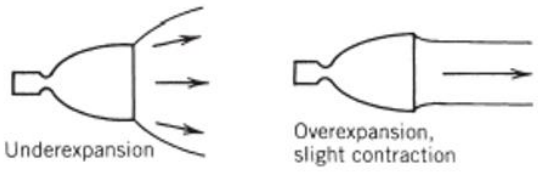

Figure 2.8: Under-Expanded and Over-Expanded Nozzle Flow Illustrations

I_{sp} is a function of the thrust, gravitational acceleration, and the mass flow rate. In Equation (2.10), I_{sp} and thrust relationship can be seen [9]. Since the increase in the nozzle throat area causes a reduction in C_F, it causes a change in the thrust. I_{sp} is directly proportional with the thrust, therefore a slight change in the nozzle throat area brings about a change in thrust and I_{sp}. In Figure 2.9 & 2.10, effect of the reduction in the nozzle throat area on I_{sp} and chamber pressure is illustrated. Chamber pressure is iterated in every 0.01 second with the new area ratios that use the 0.03, 0.06, and 0.09 mm/sec nozzle erosion rates. In table 2.1, calculation parameters are given.

$$I_{sp} = \frac{F}{\dot{m} g_0} \tag{2.11}$$

Fuel	DY12 (paraffin-based)
alpha	0.0488
n	0.62
Initial Chamber Pressure (P_c)	25 bar
Ambient Pressure (P_a)	1 bar
Oxidizer Mass Flow ($\dot{m}_{ox}$)	55 g/sec
Nozzle Regression Rate ($\dot{r_n}$)	0.03-0.06-0.09 mm/sec
Inner Fuel Diameter	32 mm
Outer Fuel Diameter	64 mm
Burn Time	15 sec
Nozzle Area Ratio	3
Throat Diameter	8.5 mm

Table 2.1: Calculation Parameters for Isp and Chamber Pressure Reduction with Different Nozzle Erosion Rates

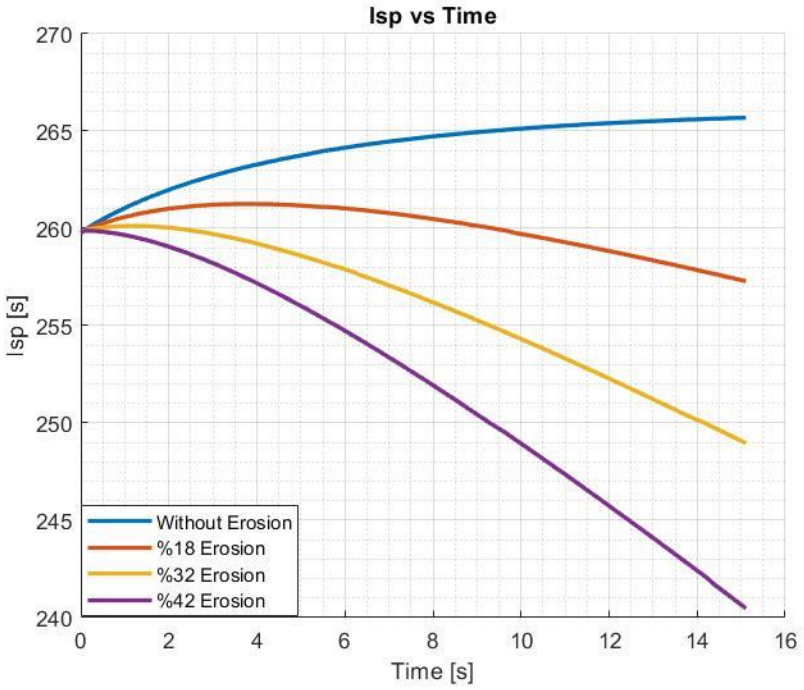

Figure 2.9: Isp Reduction with and without erosion

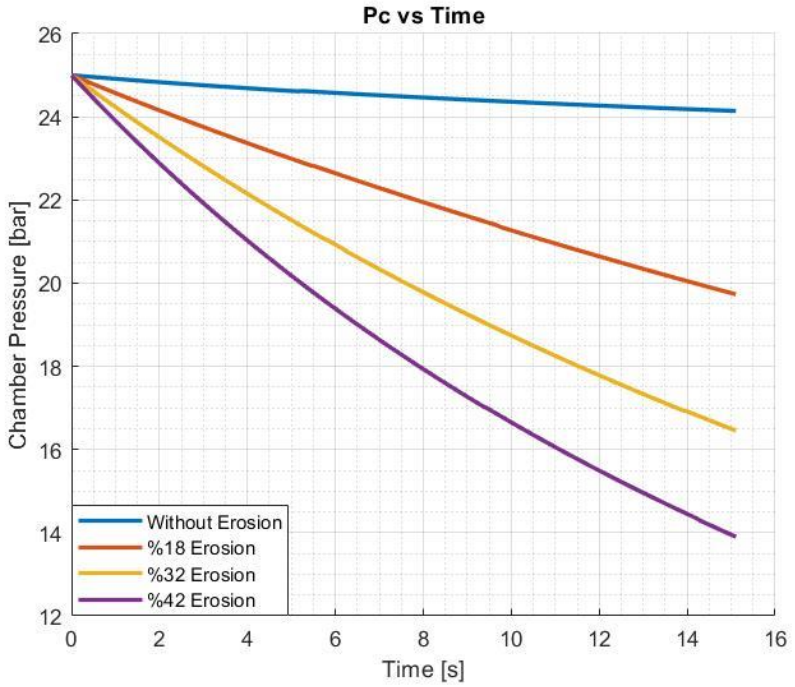

Figure 2.10: Chamber Pressure Reduction with and without erosion

2.5 *Chemical Erosion Modeling*

Chemical erosion in rocket nozzle starts with not only the oxidizing agents but also high temperature. Even if the amount of the oxidizing agents is high, at low temperatures erosion does not start. A significant erosion rate occurs with rising temperature in the presence of oxidizing species. Besides, the lack of oxidizing species at high temperatures causes no or a small amount erosion as well. The major combustion products of paraffin and GOX at the throat are H_2O, CO_2, O, OH and O_2.

In this section theoretical model of erosion is explained, but since the thesis progresses experimentally, the theoretical calculations are not specified in the thesis. The theoretical model will be studied in future studies.

2.5.1 Graphite and C/C Based Materials Heterogeneous Reactions

Heterogeneous chemical reactions are dominant at the nozzle throat since the solid particles in the combustion products are very low. There is a significant amount of oxidizing species at the nozzle throat. Besides, the temperature at the throat is nearly 2800 K. The major combustion products of paraffin and GOX at the throat are H_2O, CO_2, O, OH and O_2 and these species react with the graphite at high temperatures. In Figure 2.11, chemical reactions between the graphite and oxidizing species are shown. Erosion rate, species mass fractions at the wall, and wall temperatures are the unknowns. These unknowns can be calculated by using the diffusion boundary layer approach that Kamps et al. used in References [20] [22] [24].

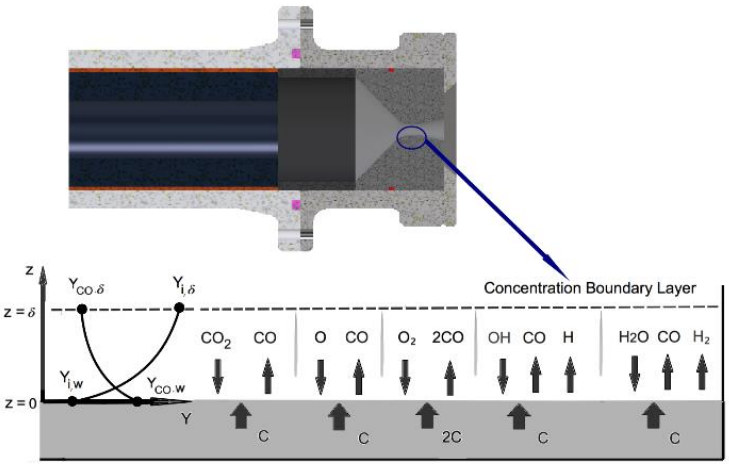

Figure 2.11: Illustration of Heterogeneous Chemical Reactions at Throat *[28]*

Erosion rate at the nozzle throat can be calculated by using Equation 2.12. Only the diffusion of only one oxidizing species "*i*" at the negative z-direction and CO at the positive z-direction are assumed in this approach.

$$\dot{r} = \sum \dot{r}_i \tag{2.12}$$

The contribution of all oxidizing species that react with the carbon at the nozzle throat surface can be calculated by using Arrhenius constants in Equation 2.13 & 2.14. 'j' is the chemical reaction order and n_j and k_j are the heterogeneous rate constants. Besides, p_i is the partial pressure (atm) of the species at the graphite wall , ρ_n is the nozzle density.

$$\rho_n \dot{r}_i = k_j p_i^{n_j} \tag{2.13}$$

$$k_j(T_w) = A_j T_w^{b_j} exp\left(\frac{-E_j}{R_u T_w}\right) \tag{2.14}$$

Where A_j, E_j, b_j are the Arrhenius empirical constants, and R_u is the universal gas constant. Constants in the Equations 2.13 & 2.14 are taken from Reference [33] [34] and can be seen in Table 2.2.

Reaction	j	ξ_i	A_j	$\frac{E_j}{R_u}, K$	b_j	n_j	*Temperature Range, K*
$C_s+H_2O\rightarrow CO+H_2$	1	3.67	480,000	34,640	0.0	0.5	800-2500
$C_s+CO_2\rightarrow 2CO$	2	1.50	9,000	34,280	0.0	0.5	800-2500
$C_s+OH\rightarrow CO+H$	3	1.42	361	0.0	-0.5	1.0	1575-1685
$C_s+O\rightarrow CO$	4	1.33	665.5	0.0	-0.5	1.0	1100-2100
$C_s+\frac{1}{2}O_2\rightarrow CO$	5a	1.33	2,400	15,107	0.0	0.0	1273-2273
	5b		21.3	-2,065	0.0	0.0	
	5c		0.0535	7655	0.0	0.0	
	5d		18,100,000	48,845	0.0	0.0	

Table 2.2: Heterogeneous Chemical Reaction Constants

The sum of all oxidizing species will give the total surface erosion mass flux. See Equation 2.15. The derivation of this equation is studied in References [35] [36].

$$\rho_n \dot{r}_i = \frac{(\rho D_{CO,i})_w}{\delta_i} \; ln\left(\frac{1+\frac{Y_{i,\delta}}{\xi_j}}{1+\frac{Y_{i,w}}{\xi_j}}\right) \tag{2.15}$$

Where D is diffusivity, δ is boundary layer thickness, ξ is the stoichiometric mass ratio for each reaction.

The binary diffusion coefficients are taken from Reference [35] (pp. 708-709) and Equation 2.16 can be written as,

$$D_{A,B} = \frac{0.0752T^{3/2}}{P\Omega(\sigma_A+\sigma_B)^2} \sqrt{\frac{1}{MW_A}+\frac{1}{MW_B}} \tag{2.16}$$

The dimensionless collision integral Ω and the dimensionless temperature T* are expressed in Equations 2.17 & 2.18. The Lennard-Jones parameters that used in these equations are given in Table 2.3 which is taken from Reference [35].

$$\Omega = \frac{1.06036}{(T^*)^{0.15610}} + \frac{0.19300}{exp(0.47635T^*)} + \frac{1.03587}{exp(1.52996T^*)} + \frac{1.76474}{exp(3.89411T^*)} \quad (2.17)$$

$$T^* = \frac{T}{\sqrt{\Lambda_A \Lambda_B}} \quad (2.18)$$

Species	σ_i, $\dot{A}$	Λ_i, K
CO	3.690	91.7
O	3.050	106.7
OH	3.147	79.8
O_2	3.467	106.7
H_2O	2.641	809.1
CO_2	3.941	195.2

Table 2.3: Lennard-Jones Parameters *[35]*

Lastly, the concentration boundary layer thickness should be calculated by using the Equation 2.19. Where Sc_i is the Schmidt number, Re is the Reynold's number and they are given in Equations 2.20&2.21.

$$\delta_i = \frac{d}{0.023 Re^{0.83} {Sc_i}^{0.44}} \quad (2.19)$$

$$Sc_i = \frac{\mu}{(\rho D_{CO,i})_w} \quad (2.20)$$

$$Re = \frac{d\rho\sqrt{\gamma RT}}{\mu} \quad (2.21)$$

The gas properties of the combustion species calculated by using the CEA. Besides, the mass fractions of the species can also be calculated. Wall temperature can be taken from the surface energy balance equation or assuming a wall temperature. Bianchi and Nasuti use a similar method in the calculations of erosion rates and the temperatures at nozzle throat [24].

$$\rho_n k_j \left(\frac{MW_{mix}}{MW_i} PY_{i,w}\right)^n = \frac{(\rho D_{CO,i})_w}{\delta_i} \ln\left(\frac{1+\frac{Y_{i,\delta}}{\xi_j}}{1+\frac{Y_{i,w}}{\xi_j}}\right) \qquad \text{for j:1 to 4} \quad (2.22)$$

$$\rho_n \left(\left(\frac{k_{5a} P_{O_2} Z_w}{1+k_{5b} Z_w} \right) + k_{5c} P_{O_2} (1 - Z_w) \right) = \frac{(\rho D_{CO,O_2})_w}{\delta_{O_2}} \; ln \left(\frac{1+\frac{Y_{O_2,\delta}}{\xi_5}}{1+\frac{Y_{O_2,w}}{\xi_5}} \right) \qquad \text{for j:5} \qquad (2.23)$$

$$(\rho v)_w = \dot{m} = \rho_s \, \dot{r} \qquad (2.24)$$

Where ρ_s is the surface density.

$$k \frac{\partial T}{\partial z}|_w + \sum_{i=1}^{N} h_{i_w} \rho D_{im} \frac{\partial y_i}{\partial z}|_w + \dot{m} h_s + q_{rad_{in}} = -k_s \frac{\partial T}{\partial z}|_s + q_{rad_{out}} + (\rho v)_w h_w \qquad (2.25)$$

Substituting the sum of surface mass balance of each species into the surface energy balance equation, Equation 2.26 can be written, and surface energy balance can be seen in Figure 2.11.

$$\underbrace{k \frac{\partial T}{\partial z}|_w}_{Convection} + \underbrace{q_{rad_{in}}}_{Radiation\ in} = \underbrace{\sum_{i=1}^{N} \dot{w} h_{i_w} - \dot{m} h_s}_{Ablation} + \underbrace{q_{rad_{out}}}_{Radiation\ out} - \underbrace{k_s \frac{\partial T_s}{\partial z}|_s}_{Solid\ Conduction} \qquad (2.26)$$

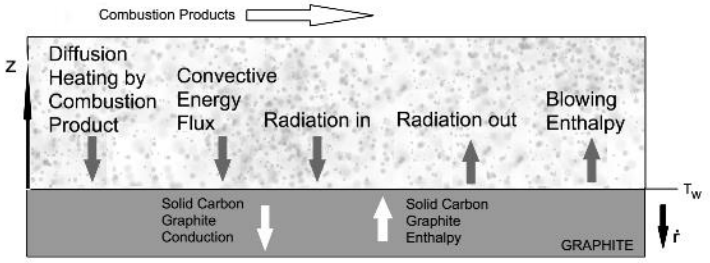

Figure 2.12: Surface Energy Balance at Nozzle Throat *[28]*

Convective heat transfer in the Equation 2.26 is calculated by using the Bartz equation which is given in Reference [37]. Radiative heat transfer is neglected due to its small value.

At the nozzle throat, steady-state assumption is made since the temperature at the surface increases quickly. Besides, the heat transfer to the surface along the nozzle is neglected, only the heat transfer that is in the radial direction is taken. Therefore, the heat transfer at the nozzle throat can be written as it is in the Equation 2.27.

$$\rho_n \frac{\partial h_s}{\partial t} = \frac{\partial}{\partial r} \left(k_s \frac{\partial T_s}{\partial r} \right) + \rho_n r \frac{\partial h_s}{\partial r} \qquad (2.27)$$

Nozzle temperature can be calculated by using Equations 2.2 & 2.29 by making constant heat capacity and conduction assumption.

$$T(r) = -C \frac{\kappa}{\dot{r}} e^{\frac{-\dot{r} r}{\kappa}} + 300 \qquad (2.28)$$

$$\kappa = \frac{k}{\rho C_p} \tag{2.29}$$

Finally, by using all these equations above, erosion rates of each species can be calculated. The equations should be thought as in a body and the effects of all combustion species should also be considered.

2.5.2 Tungsten Heterogeneous Reactions

Tungsten is a suitable material due to its high melting temperatures. Although the endurance of Tungsten at high temperatures, its high cost and density restrain its use as a nozzle material.

Chemical reactions at the nozzle throat surface which use Tungsten as nozzle material can occur at high temperatures. There are a significant number of studies about the use of Tungsten as a nozzle material and its reactions with the combustion products. In Reference [38], Thakre stated that the combustion products such as CO and H_2 do not react with tungsten unlike H_2O and CO_2 [39]. In addition to this, Batchelor et al. proved that the in the presence of CO and H_2 reactions between W and H_2O & CO_2 decrease. Thus, erosion rates at the nozzle throat decrease as well [40].

In the research about the oxidation of Tungsten, Walsh stated that the main product in the reaction of tungsten and steam is WO_2. On the other hand, Batchelor suggested that the main product is WO_3 [40] [41]. Belton et al. observed that the $WO_3H_2O_{(g)}$ occurs with the reaction of H_2O and WO_3 which reduces the H_2O amount in the combustion products. Therefore, the amount of chemical erosion due to H_2O is reduces as well [42].

	H_2O	$WO_{3(l)}$	WO_3 and its polymers	H_2	WO_2	ΔH_R	ΔG_R
W/H_2O	0.35	0.12	0.51	0.02	0	-2910.20	-23939.10
	CO_2	$WO_{3(l)}$	WO_3 and its polymers	CO	WO_2	ΔH_R	ΔG_R
W/ CO_2	0.14	0.42	0.21	0.23	0	-2285.98	-13354.6

Table 2.4: Chemical Equilibrium Calculations for W/CO2 and W/H2O *[38] [39]*

The values in Tables 2.4 & 2.5 are taken from references [38] and [39]. Reactants in the tables are at 2800 K and 40 atm with a mass ratio of 1:1.

Reaction at Nozzle Surface	A_i	E_i	$\dot{\omega}_i$	Temperature Range
$W + 3H_2O_{(g)} \rightarrow WO_{3(g)} + 3H_{2(g)}$	8.64	22.70	$k_i p_{H_2O}$	1723-1973
Or	5.722×10^4	48.13	$k_i p_{H_2O}$	1073-1973
$W + 2H_2O_{(g)} \rightarrow WO_{2(g)} + 2H_2$	1.433×10^4	47.23	$k_i p_{H_2O}$	1073-1623
$W + 3CO_{2\,(g)} \rightarrow WO_{3(g)} + 3CO_{(g)}$ Or $W + 2CO_{2\,(g)} \rightarrow WO_{2(g)} + 2CO_{(g)}$	4.026×10^3	79.00	$k_i p_{CO_2}^{0.88}$	2200-3200

Table 2.5: Heterogeneous Chemical Reaction Constants of Tungsten

A_i in kg/m^2-s-atm for the first reaction and kg/m^2-s-torr$^{0.88}$ for the second reaction. E_i is in kcal/mol, $\dot{\omega}_i$ is in kg/m^2-s, and temperatures are in K. Values are taken from References [38] [41] [43] [44] [45]. Using equations that are given in the Section 2.5.1 and these values heterogeneous chemical reactions can be written and erosion rates can be calculated.

2.5.3 Molybdenum Heterogeneous Reactions

Molybdenum is a remarkable material since its durability at high temperatures. However, low oxidation temperature and brittle structure of molybdenum limits its use in hybrid rocket motors due to the high amount of oxidizing species in HRMs. In References [46] [47], the main products from the oxidation of Molybdenum are $H_{2(g)}$ and $MoO_{3(g)}$, and its polymers. Due to the lack of the studies about the reaction of CO_2 and Mo, Thakre gave the heterogeneous chemical reactions values of only the reaction between Mo and H_2O [38].

	H_2O	$Mo_{(c)}$	MoO_3 and its polymers	H_2	ΔH_R	ΔG_R
Mo/H_2O	0.36	0.26	0.36	0.015	-2497.07	-24292.3
	CO_2	$Mo_{(c)}$	MoO_3 and its polymers	CO	ΔH_R	ΔG_R
Mo/ CO_2	0.15	0.25	0.38	0.22	-1828.15	-13692.9

Table 2.6: Chemical Equilibrium Calculations for Mo/CO2 and Mo/H2O *[38] [39]*

Reaction at Nozzle Surface	A_i	E_i	$\dot{\omega}_i$	Temperature Range
$Mo + 3H_2O_{(g)} \rightarrow MoO_{3(g)} + 3H_{2(g)}$	4.48	57.5	$k_i p_{H_2O}$	1373-1973

Table 2.7: Heterogeneous Chemical Reaction Constants of Molybdenum *[38] [47]*

2.5.4 Oxidation Behavior of Silicon Carbide

Silicon carbide is a novel material for rocket nozzles due to its low density, high strength, high hardness, and excellent thermal shock resistance. Oxidation behavior of silicon carbide can be both active and passive. In Reference [48] [49], passive oxidation of SiC is given as;

$$2SiC + 3O_2 \rightarrow 2SiO_2 + 2CO \uparrow \quad (2.30)$$

In this reaction, a protective layer consists of the nozzle surface which is usually silica. Weidenmann et al. stated that in the passive oxidation of SiC, there are two main oxidation mechanisms. First is parabolic oxidation which is controlled by the oxidizing products through the silica layer. In parabolic oxidation process, diffusion rate is assumed as constant. On the other hand, in non-parabolic oxidation process, diffusion rate is time dependent [48]. Weidenmann et al. stated that the active oxidation causes erosion on the surface material. Active oxidation reactions of SiC can be seen in Equation 2.31 & 2.32 & 2.33.

$$SiC + O_2 \rightarrow SiO \uparrow + CO \uparrow \quad (2.31)$$

$$2SiC + 3O_2 \rightarrow 2SiO_2 + 2CO \uparrow \quad (2.32)$$

$$SiO_2 + 2H_2O \rightarrow 2Si(OH)_4 \uparrow \quad (2.33)$$

Roy et al. stated that oxide layer thickness is increases with rising temperature [49] [50]. In Equation 2.34, the formula for calculation of the thickness of the oxide layer on the surface of SiC can be seen.

$$t = \frac{\Delta E}{|\varepsilon|_{si} N} \quad (2.34)$$

Where ΔE is the energy difference between two layers, N is the number of silicon atoms, and $|\varepsilon|_{si}$ is the stopping cross section factor for silicon.

In conclusion, during the active oxidation, the strength of the SiC reduces linearly. Unlike the active oxidation, passive oxidation protects the surface of the SiC due to the

formation of the oxide layer on the surface. Therefore, passive oxidation makes the SiC more durable to the oxide attacks.

2.6 Factors that Affect Nozzle Erosion

2.6.1 Effect of Throat Length

In the design of nozzle, 15-degree divergent angle is used and radius of curvatures are given by using Rao contour [51]. Convergent section angle hardly ever affects the nozzle erosion rates, but in this study, effect of the nozzle throat length is investigated.

Three different nozzles that had various throat lengths are tested at the same conditions to compare them each other. 0.8 mm, 2.8 mm, 4.8 mm, 6.8 mm, 8.8 mm, and 9.8 mm throat lengths were tested. Graphites are manufactures by using Grade 1. It was observed that the erosion decreased as the length increased. However, it has been observed that erosion rates begin to increase when the length to diameter (L/D) ratio exceeds almost 1. In large scale motors, L/D effect may be different, so this L/D ratios should be considered for only this scale.

In Table 2.8, test results are shown. In test results, 4.8_3 was outlier, therefore this test repeated and erosion rates of 4.8_3 accepted. In Figure 2.13, erosion rates at different throat lengths are given.

Table 2.8:Different Throat Length Nozzles Test Results

Material	t_{burn} (sec)	P_{cavg} (bar)	O/F	$D_{t(i)}$ (mm)	$D_{t(f)}$ (mm)	Erosion Onset (sec)	Erosion Rate (mm/sec)
0.8_1	11.89	21.48	2.55	7.15	8.94	2.99	0.1006
0.8_2	11.88	21.59	2.5	7.15	9.02	3.00	0.1053
2.8_1	11.9	22.41	2.59	7.11	8.498	3.80	0.0857
2.8_2	11.9	22.06	2.76	7.11	8.465	3.70	0.0826
4.8_1	11.85	19.81	2.67	7.11	9.21	2.08	0.1075
4.8_2	11.9	22.41	2.66	7.11	8.194	4.39	0.0722

4.8_3	11.87	21.59	2.68	7.05	8.635	1.88	0.0793
6.8_1	11.8	23.18	2.53	7.05	8.474	4.5	0.0975
6.8_2	11.86	21.8	2.68	7.03	8.744	2.52	0.0918
8.8	11.76	23.12	2.54	7.05	8.35	3.26	0.0765
9.8_1	11.82	22.68	2.5	7.00	8.37	3.07	0.0783
9.8_2	11.85	21.28	2.6	7.00	8.74	2.06	0.0889

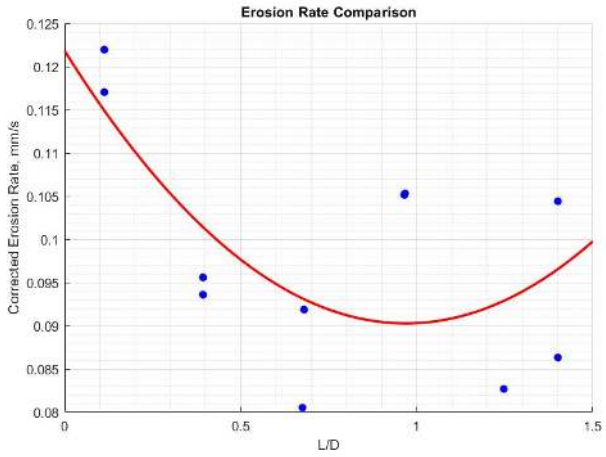

Figure 2.13: Erosion Rates vs Throat Length - Grade 1

2.6.2 Motor Parameters

O/F Ratio

The most dominant motor parameter that affects the erosion rates is O/F ratio. Nozzle erosion increases at high O/F ratios due to the high number of oxidizing species in the combustion products. In Chapter 4, erosion rates of different graphite types at various O/F ratio are given.

Pressure

Pressure has a slight effect on the erosion rates of nozzle. When pressure is high there is more heat flux at the throat which increases the nozzle erosion rates. Grade 1 test results were compared with respect to chamber pressure and a slight pressure effect on erosion rates were observed. O/F ratios of the tests in the graph are between 2.3 and 2.5.

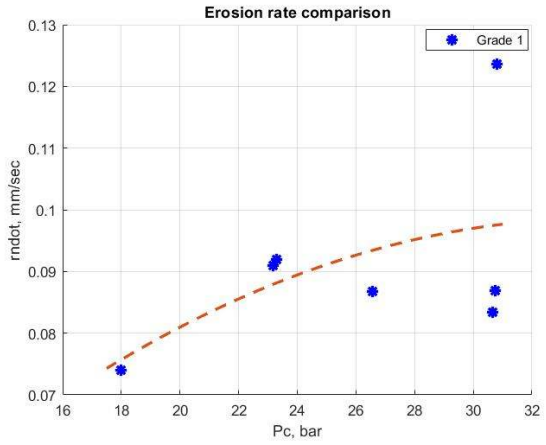

Figure 2.14: Erosion Rates vs Chamber Pressure

2.6.3 Fuel Formulation

Karakas et al. stated that the addition of micro aluminum to the paraffin-based fuel has a great effect on the erosion rates. 10 % aluminum powder addition to the fuel reduces the erosion rates as much as possible [26] [28]. Al_2O_3 formation occurs between the aluminum in the fuel and the oxidizer, so the amount of the oxidizing agents decreases. Therefore, due to the lack of free oxygen, chemical reactions between the nozzle material and the combustion products are diminished [26]. Moreover, metallic powders such as $LiAlH_4$, NBH_6, and Mg also cause a significant reduction in the nozzle erosion rates. Even though, $LiAlH_4$ and NBH_6 have a positive impact on the performance of the rocket motor, they are not preferred due to their high costs [27] [28]. See Figures 5 to see the effect of metallic powders on the nozzle erosion rates. In Figure 2.4, oxidizer is liquid N_2O and in Figure 2.15 the oxidizer is GOX.

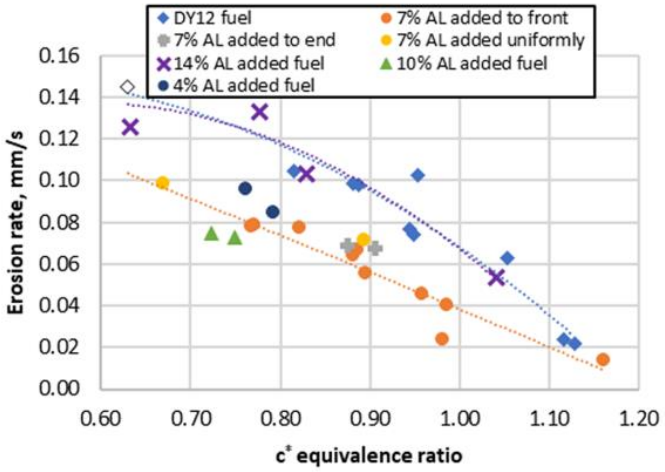

Figure 2.15: Erosion Rates vs Eq. Ratios for Different Fuel Formulations *[28]*

2.7 Nozzle Erosion Minimization Techniques

Nozzle erosion is one of the most important factors in because of the extreme conditions in HRMs' combustion chambers. In the nozzle, especially at the throat region, heat mass fluxes are higher than the other parts of the rocket. Temperatures can reach nearly 2800 K at the nozzle throat, therefore, if this situation is paired with the high amount of oxidizing agents in the combustion products, nozzle erosion is inevitable [13].

In addition to the performance parameters (I_{sp}, regression rate) discussed above, thrust profile is also an essential parameter in rocket propulsion systems. The nozzle design is a critical parameter in predicting thrust profile. Since the reduction of the nozzle area ratio causes I_{sp} loss, the nozzle area ratio variation affects the rocket engine's thrust. Mechanical and chemical erosions in the nozzle throat can cause changes in the rocket nozzle area ratio. Temperatures at the nozzle throat due to the combustion at high temperatures and pressure can be considerably high and reach 3000-3500 K. Due to high mass fractions of oxidizing agents in hybrid and liquid rocket motors, chemical erosion is much more than in solid rocket motors. Propellant combinations should not contain more than an acceptable amount of free oxygen due to high reactiveness at high temperatures. Therefore, the O/F ratio plays a vital role in the nozzle erosion of liquid and hybrid rocket motors and running at low oxidizer-to-fuel ratios can decrease nozzle erosion rates. In addition, chamber pressure is one of the critical parameters for nozzle erosion. Operating at low chamber pressures can be a good choice since high chamber pressures increase nozzle mass flux and heat transfer, which speeds up nozzle erosion. Another option for minimizing nozzle erosion can be formulating fuels by reducing mass fractions of oxidizing species. For example, metal additives to the hybrid rocket fuels such as aluminum (AL), magnesium (Mg), ammonium borane (BH_3NH_3), or lithium aluminum hydride ($LiALH_4$) can decrease nozzle erosion rate [27]. The most important factor that minimizes nozzle erosion is selecting suitable nozzle material [13]. Materials that have been used in hybrid rocket propulsion systems can be determined in different groups [52]:

1) Carbon-based materials (Graphite, C-C composite)
2) Metals (Tungsten, tantalum, molybdenum, rhenium)
3) Ceramics (Silicon Carbide, Hafnium Carbide, Tungsten Carbide)
4) Polymer composites (Silica glass, carbon fibers)

In carbon-based materials, graphite is a better material for hybrid rocket motors due to its better durability (with respect to C-C composites) for oxygen attacks. On the other hand, C-C increases the mechanical strength of the nozzle. Therefore, it is more suitable for solid rocket motors since they are exposed to solid particle attacks [13].

Metals can be used due to their low chemical reaction possibility and high resistance to mechanical impacts and heat. Machinability of metals such as tungsten and tantalum are not easy; thus, they are not preferred much. Since ceramics are resistant to high temperatures, they can be preferred as nozzle material. They are not very common due to the difficulty of the production process and sometimes cost-effectiveness [13].

Chapter 3:
DESIGN AND TESTING OF HYBRID ROCKET MOTOR

3.1 Motor Design

A hybrid rocket motor that has 65 mm outer paraffin-based fuel grain diameter and GOX are used for this study. Motor parameters are calculated by using NASA Chemical Equilibrium with Applications. Chamber pressure, nozzle throat diameter, area ratio, fuel dimensions are given as initial conditions. Regression rate is calculated by using the Equation 3.2 from Reference [17].

$$\dot{r} = \alpha {G_{ox}}^{n} \tag{3.1}$$

Karabeyoglu gives α and n constants for oxygen & paraffin-based fuels in reference 17. Therefore, Equation 3.1 can be written as,

$$\dot{r} = 0.117 {G_{ox}}^{0.62} \tag{3.2}$$

In internal ballistics calculations, chamber pressure is updated in every 0.01 sec by using Equation 3.3 due to the change in nozzle area, c*, and mass flow rate.

$$P_c = \frac{c^* \dot{m}}{A_t} \tag{3.3}$$

Where c* is characteristic velocity, $\dot{m}$ is the total mass flow rate, and A_t is the nozzle throat area.

Different mass flow rates and grain lengths are used to change the O/F ratio because the O/F is the most critical parameter for nozzle erosion. Different grain lengths give us the opportunity to do the test with varying O/F ratios. Motor configuration with a length of 250 mm fuel design can be seen in Figure 3.1 and 3.2.

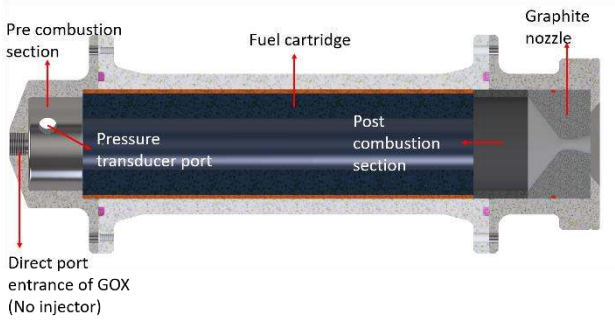

Figure 3.1:Hybrid Rocket Motor Design That Used in This Study *[28]*

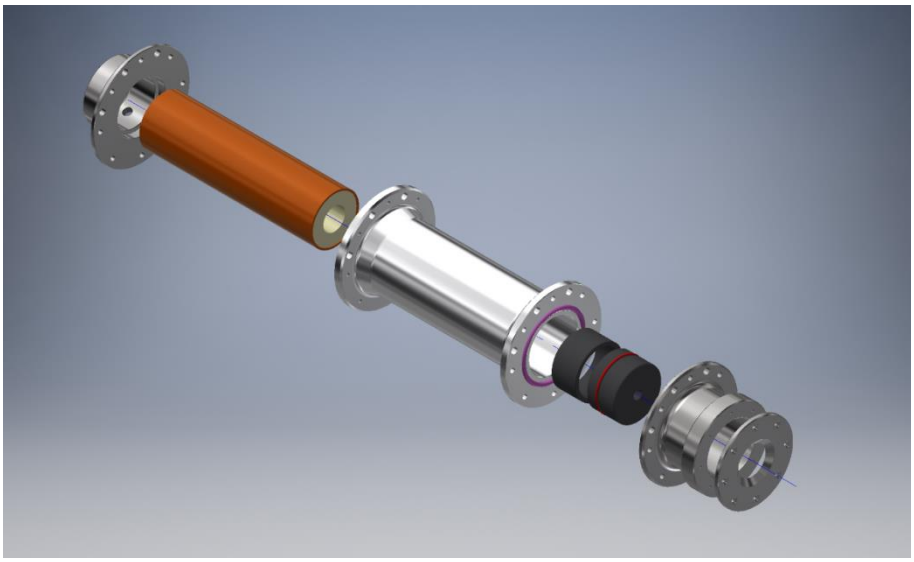

Figure 3.2: Hybrid Rocket Motor Design *[13]*

3.2 Experimental Test Setup

Experimental test set-up with GOX and paraffin-based fuel (DY12) can be seen in Figure 3.2. The outer casing of the motor is made of aluminum, and front and aft motor casings are made of steel. GOX is taken from a run tank and injected from a 3/8 inches pipe through the motor without an injector.

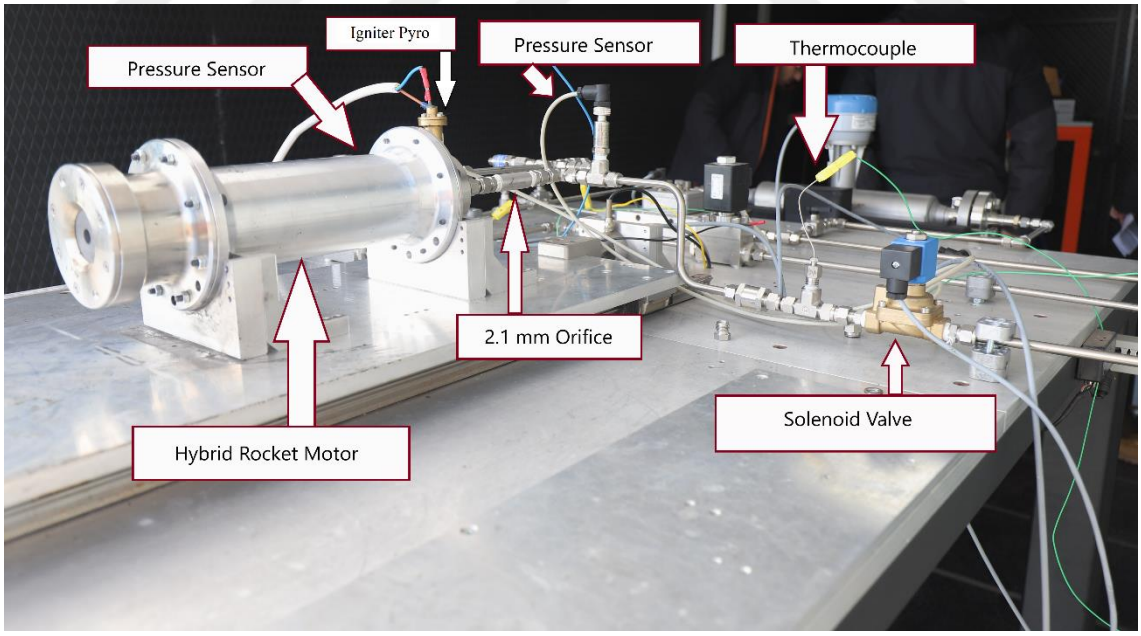

Figure 3.3: Experimental Test Setup

To start the ignition, a solid propellant pyrotechnic igniter is used, and ignition starts by sending current to the pyrotechnic igniter. 2.1 mm orifice is used to choke the flow before the motor entry and the oxidizer mass flow rate is calculated from the data

temperature that was taken from the thermocouple and pressure transducer in the oxidizer line. K type thermocouple was used to measure the line temperature. Data in the tests are recorded by the National Instruments Data Acquisition System and Lab View software. The DAQ sampling rate during the tests was 5120 Hz. A 70-bar pressure transducer that has +/- 0.5% efficiency was used to measure line before and after the orifice and the chamber. In Reference [28], a relative error analyses for this test experiments was given.

Tests were performed with varying pressures and O/F ratios to obtain different erosion rates. Therefore, different nozzle throat diameters were used to change the chamber pressure. Although, changing the mass flow rate is also an option to change chamber pressure, for the optimal conditions one of them was preferred. See the Table 3.1 to find test parameters.

Fuel	DY12 (paraffin-based)
Oxidizer to Fuel Ratio (O/F)	1.5-4.5
Chamber Pressure (P_c)	18-35 bar
Oxidizer Mass Flow ($\dot{m}_{ox}$)	20-100 kg/m^{2}sec
Fuel Mass (M_f)	0.3-0.7 kg
Nozzle Regression Rate ($\dot{r_n}$)	0.02-0.4 mm/sec
Thrust (T)	110-350 N
Burn Time	7 to 20 sec
Combustion Efficiency	%87-95

Table 3.1: Test Parameters *[13]*

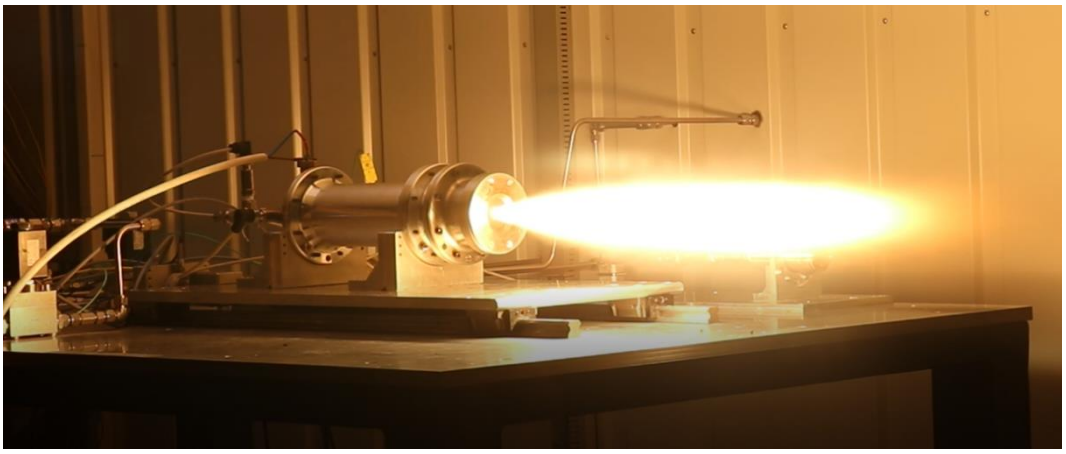

Figure 3.4: Example Hot Firing Test

Chapter 4:
MATERIAL PERFORMANCES AND TEST RESULTS

In this section, test results of each material were given. Maximum number of tests were done by using Grade 1, therefore curves of the test results in Grade 1 is more sensible. Even though the curves are not fit for each material since there are some outliers, graphs of each graphite were given. For the other materials, test results were given in tables.

4.1 Graphites

This study mainly focusses on the erosion rates of the graphite nozzles. Five different graphite grades were tested at various oxidizer to fuel ratios. Using the test results, their erosion rates and onsets were investigated. The properties of graphite that affect the erosion rates are grain size, ash content, thermal conductivity, porosity, and the thermal expansion coefficients. There is a linear correlation between the grain sizes and the erosion rates if they are tested at the same conditions. Not only the grain size affects the erosion rates, but also conductivity has a significant effect on erosion rates. Erosion rates generally decreases with rising thermal conductivity. Surface temperature of the nozzle with a material that has high thermal conductivity remains cooler due to its rapid heat transfer to the outer casing. Therefore, reactions at the nozzle surface start later and erosion onset time increases. In this section, properties and test results of various graphite grades are given. Erosion rates and onsets are given with respect to the O/F and Equivalence ratios. Since, each of the tests have done at different chamber pressures, erosion results are corrected for a 25-bar reference chamber pressure.

$$\dot{\bar{r}}_{n_{corrected}} = \dot{\bar{r}}_n \frac{P_{c\,ref}}{P_c} \tag{4.1}$$

4.1.1 Grade 1 Specifications

Table 4.1: Graphite Grade 1 Properties

Grade	Grain Size	Porosity	Ash Content	CTE (400-500°C)	Thermal Conductivity	Density
1	8 μm	7 %	400 ppm	6,0 x10E-6/°C	105 W/m°C	1,84 g/cm^3

In Figures 4.1&4.2 erosion rate results of Grade 1 graphite are shown with respect to the O/F ratio. In Figures 4.3&4.4 erosion rate results of Grade 1 graphite are shown with respect to the equivalence ratios. Finally, in Figures 4.5&4.6, erosion onset times with respect to O/F and equivalence ratios are given.

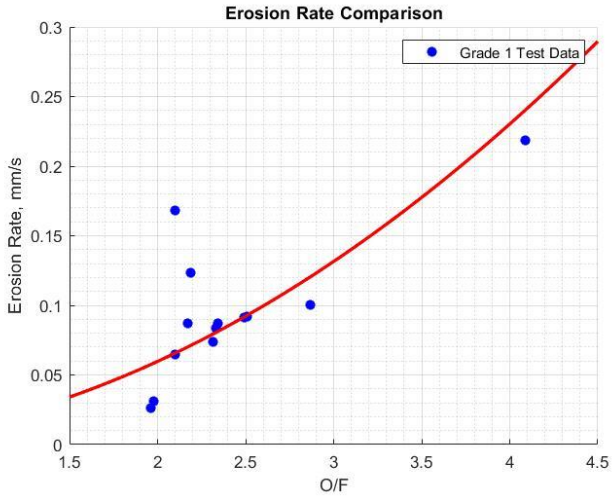

Figure 4.1: Erosion Rates vs O/F - Grade 1

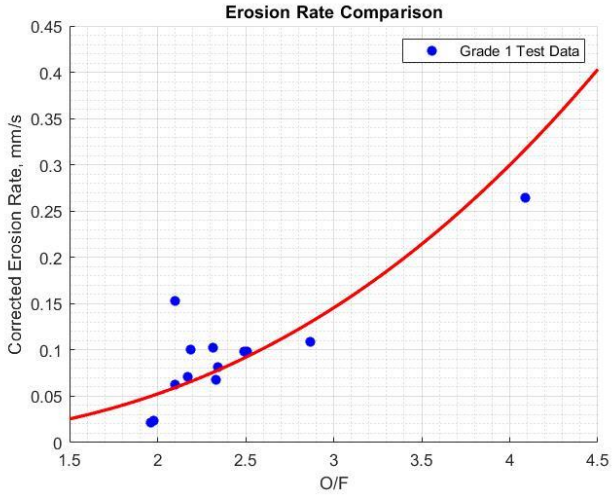

Figure 4.2: Corrected Erosion Rates vs O/F - Grade 1

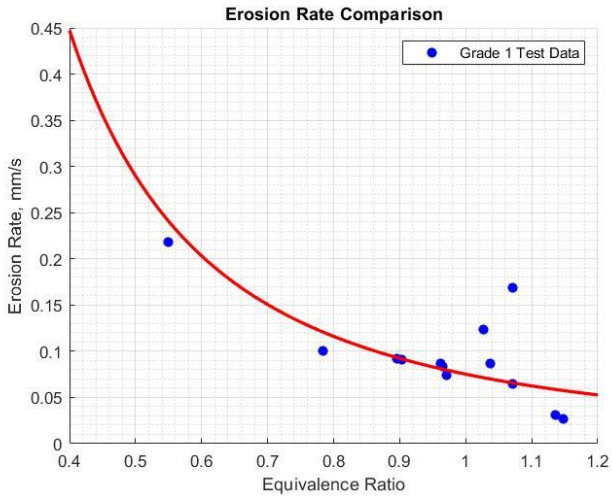

Figure 4.3: Erosion Rates vs Equivalence Ratios - Grade 1

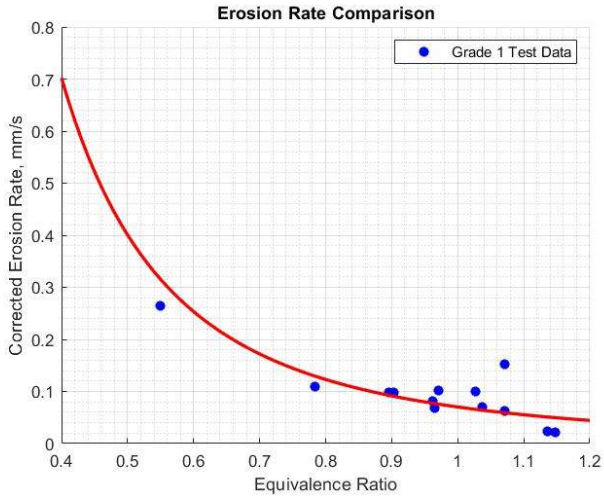

Figure 4.4: Corrected Erosion Rates vs Equivalence Ratios - Grade 1

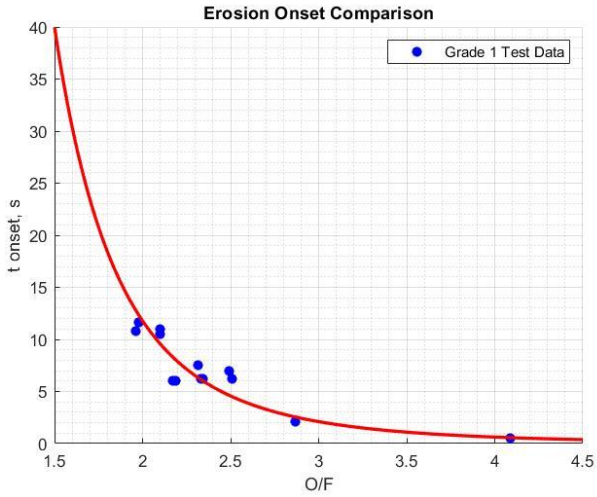

Figure 4.5: Onset Times vs O/F - Grade 1

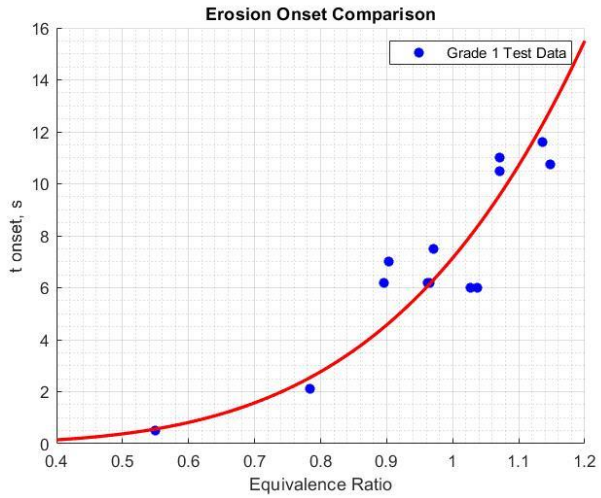

Figure 4.6:Onset Times vs Equivalence Ratios - Grade 1

4.1.2 Grade 2 Specifications

Table 4.2: Graphite Grade 2 Properties

Grade	Grain Size	Porosity	Ash Content	CTE (400-500°C)	Thermal Conductivity	Density
2	9 µm	8 %	300 ppm	5,6 x10E-6/°C	106 W/m°C	1,83 g/cm^3

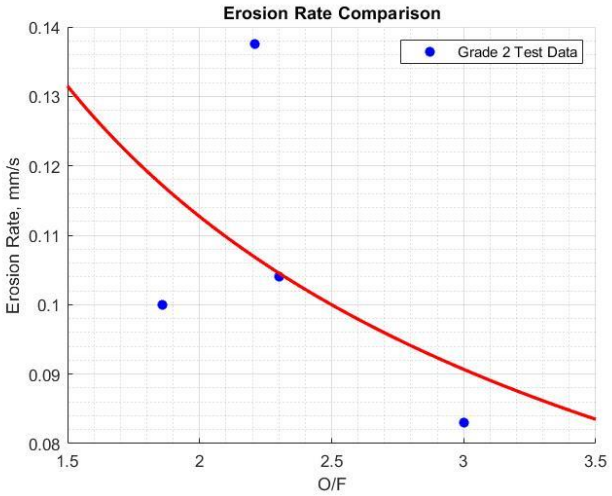

Figure 4.7: Erosion Rate vs O/F - Grade 2

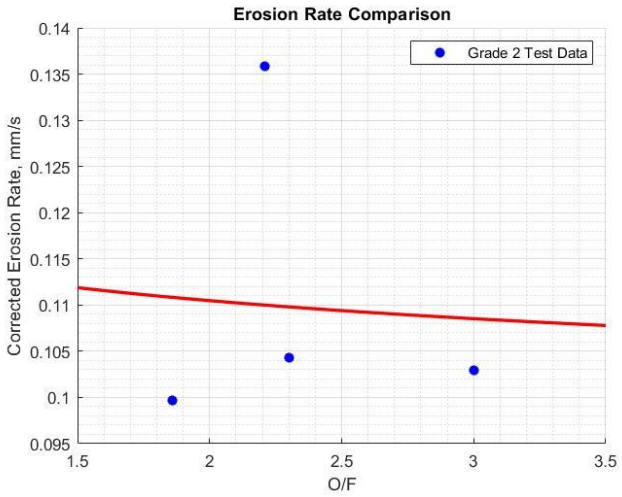

Figure 4.8: Corrected Erosion Rates vs O/F – Grade 2

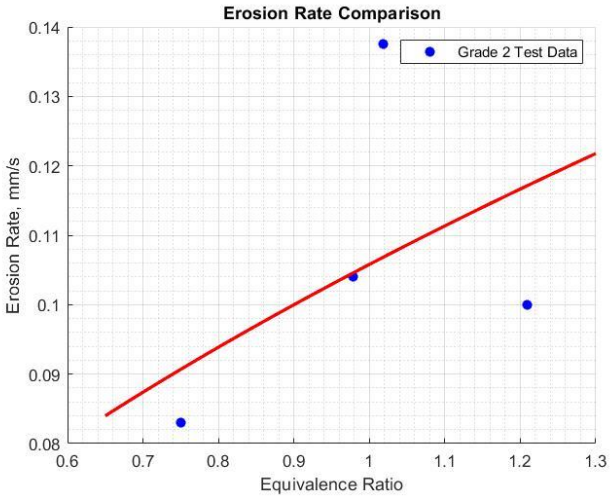

Figure 4.9: Erosion Rates vs Equivalence Ratios – Grade 2

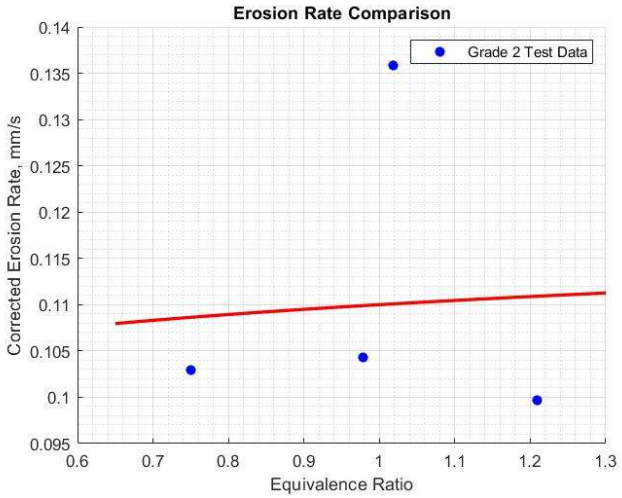

Figure 4.10: Corrected Erosion Rates vs Equivalence Ratios - Grade 2

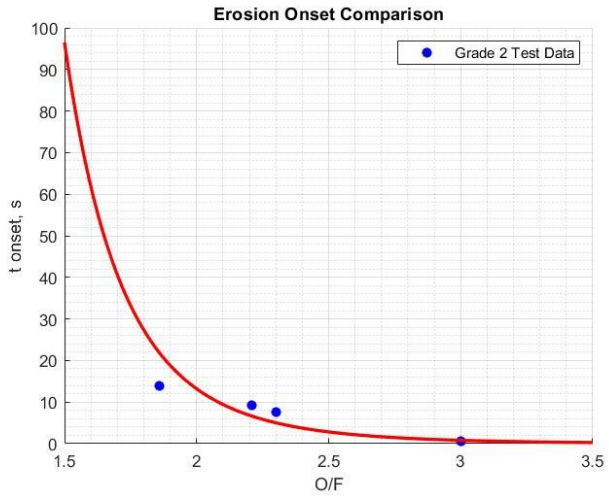

Figure 4.11: Onset time vs O/F - Grade 2

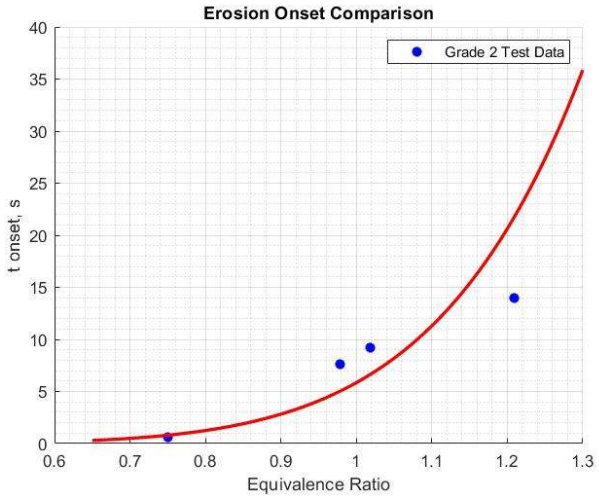

Figure 4.12: Onset Time vs Equivalence Ratios - Grade 2

4.1.3 Grade 3 Specifications

Table 4.3: Graphite Grade 3 Properties

Grade	Grain Size	Porosity	Ash Content	CTE (400-500°C)	Thermal Conductivity	Density
3	13 µm	12 %	300 ppm	5,2 x10E-6/°C	95 W/m°C	1,7 g/cm^3

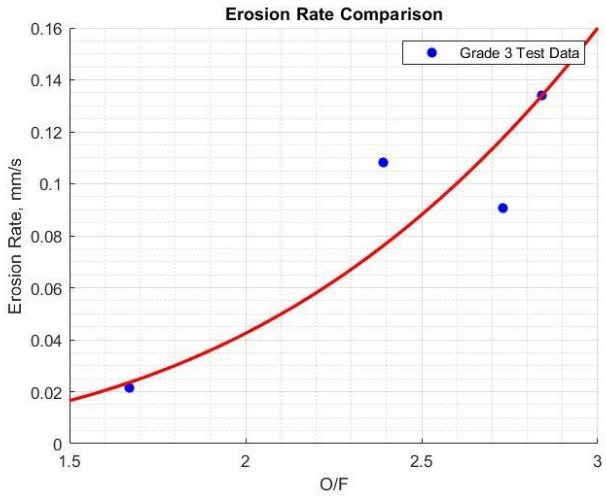

Figure 4.13:Erosion Rate vs O/F - Grade 3

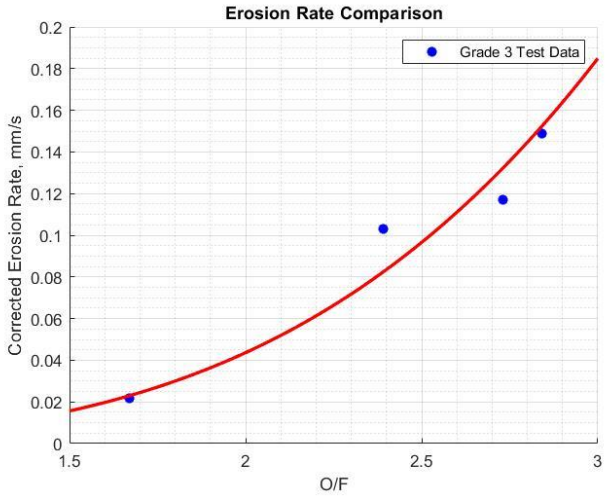

Figure 4.14: Corrected Erosion Rates vs O/F – Grade 3

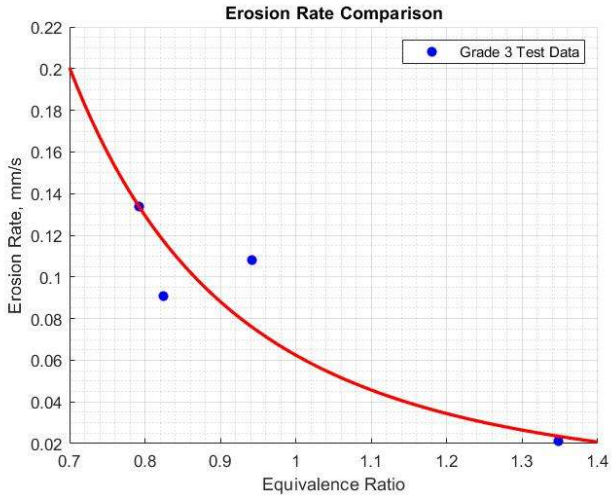

Figure 4.15: Erosion Rates vs Equivalence Ratios – Grade 3

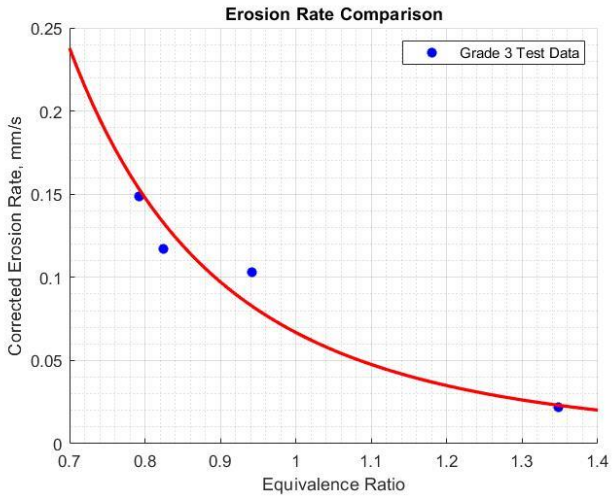

Figure 4.16: Corrected Erosion Rates vs Equivalence Ratios - Grade 3

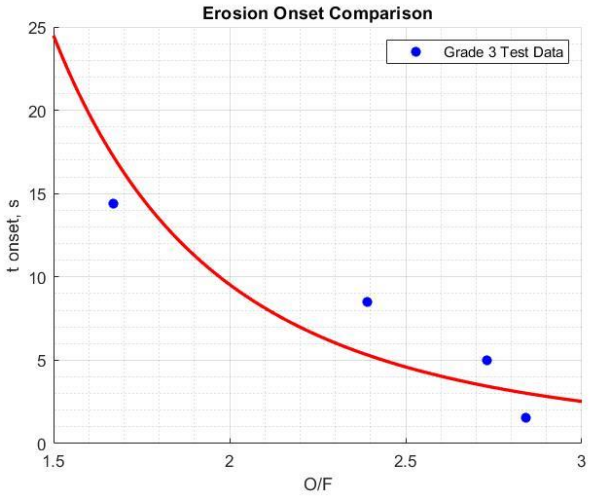

Figure 4.17: Onset time vs O/F - Grade 3

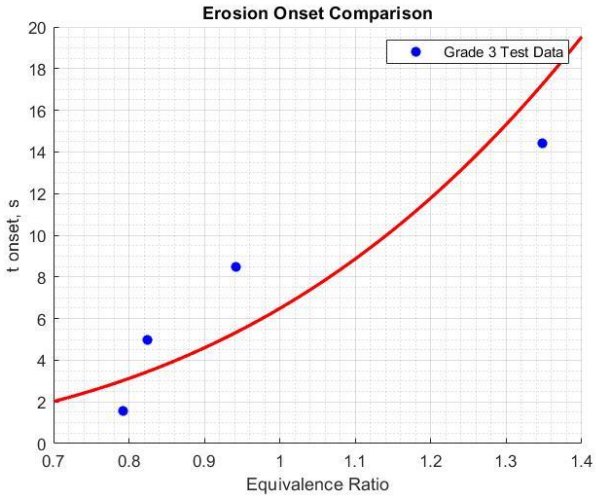

Figure 4.18: Onset Time vs Equivalence Ratios - Grade 3

4.1.4 Grade 4 Specifications

Table 4.4: Graphite Grade 4 Properties

Grade	Grain Size	Porosity	Ash Content	CTE (400-500°C)	Thermal Conductivity	Density
4	15 µm	9 %	750 ppm	4,3 x10E-6/°C	85 W/m°C	1,77 g/cm^3

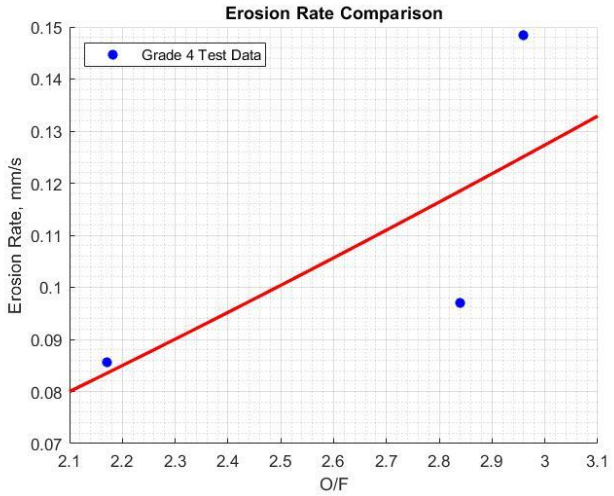

Figure 4.19: Erosion Rate vs O/F - Grade 4

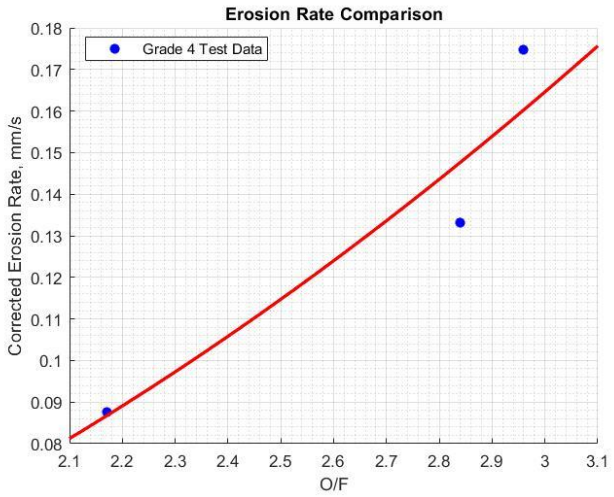

Figure 4.20: Corrected Erosion Rate vs O/F - Grade 4

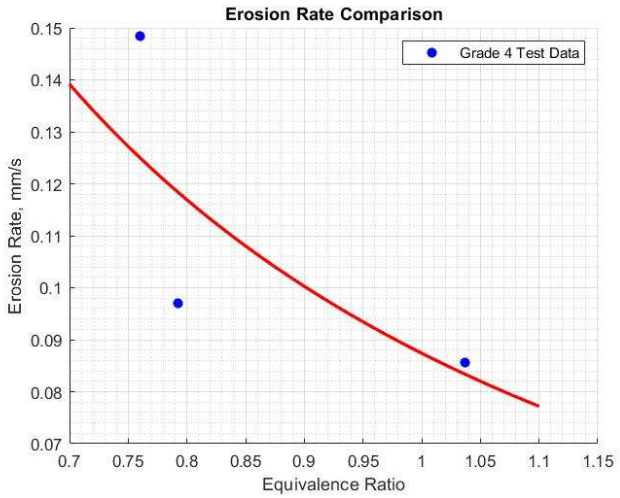

Figure 4.21:Erosion Rates vs Equivalence Ratios – Grade 4

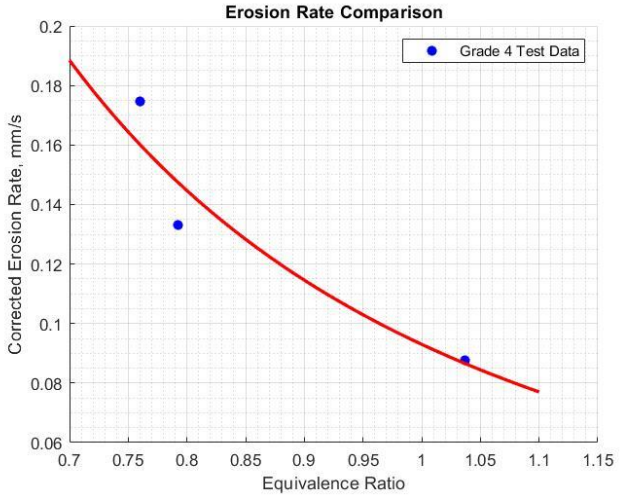

Figure 4.22: Corrected Erosion Rates vs Equivalence Ratios – Grade 4

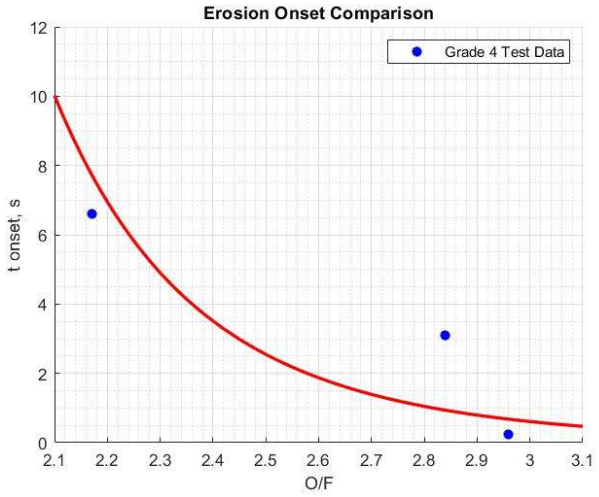

Figure 4.23: Onset time vs O/F - Grade 4

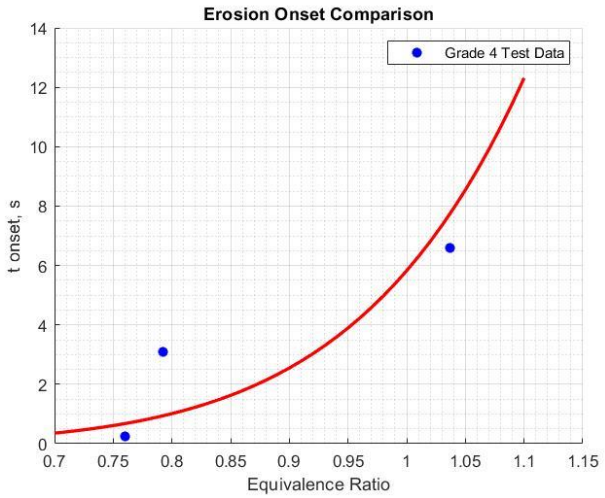

Figure 4.24: Onset Times vs Equivalence Ratios - Grade 4

4.1.5 Grade 5 Specifications

Table 4.5: Graphite Grade 5 Properties

Grade	Grain Size	Porosity	Ash Content	CTE (400-500°C)	Thermal Conductivity	Density
5	4 µm	-	400 ppm	7,5 x10E-6/°C	120 W/m°C	1,88 g/cm^3

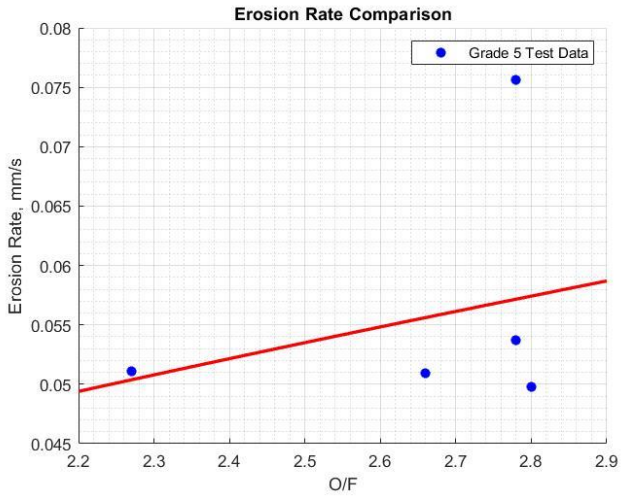

Figure 4.25: Erosion Rates vs O/F - Grade 5

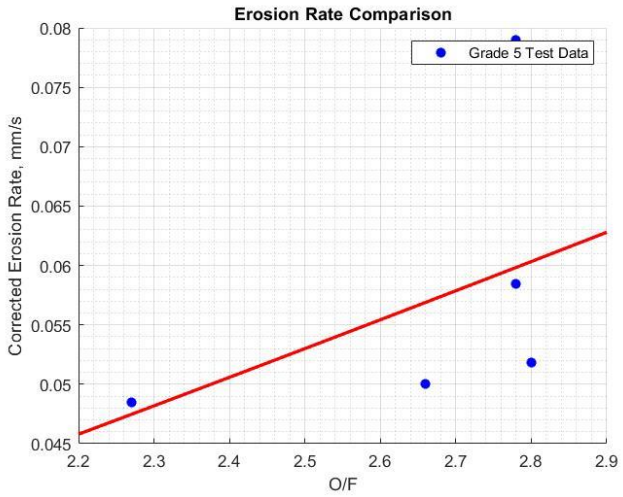

Figure 4.26:Corrected Erosion Rates vs O/F - Grade 5

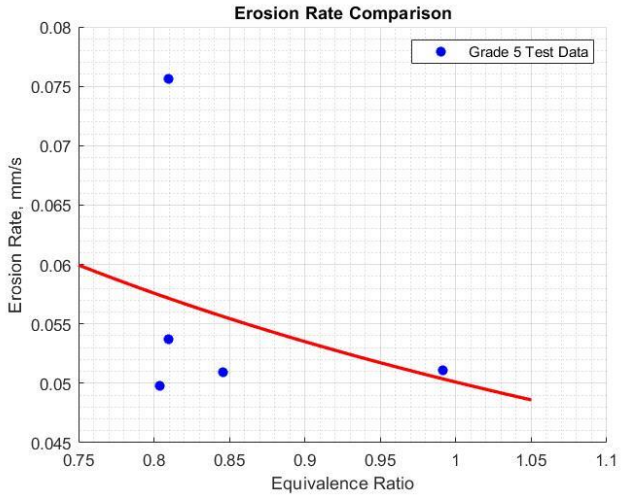

Figure 4.27: Erosion Rates vs Equivalence Ratios - Grade 5

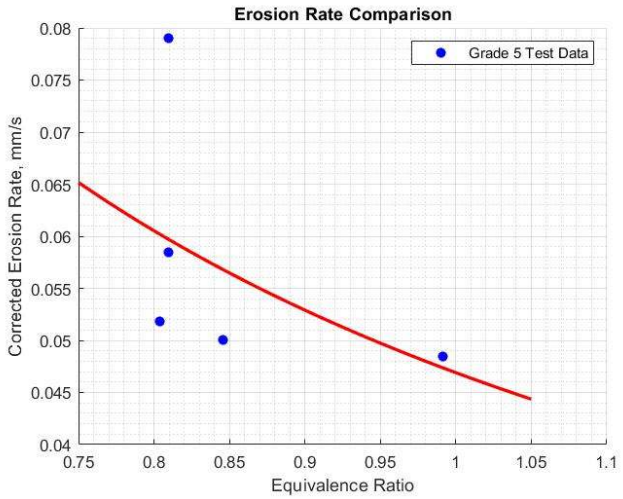

Figure 4.28: Corrected Erosion Rates vs Equivalence Ratios - Grade 5

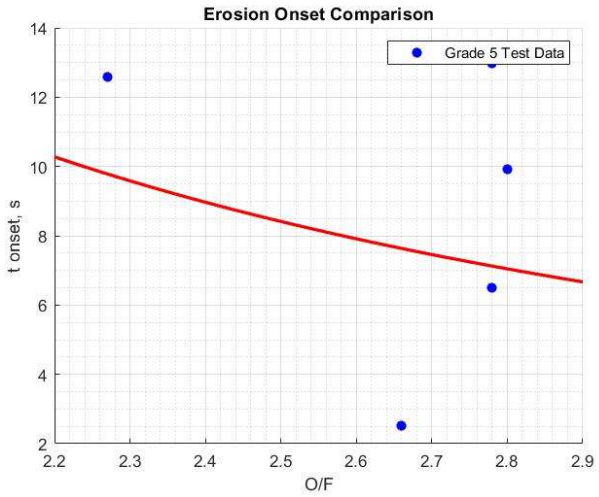

Figure 4.29: Onset Time vs O/F - Grade 5

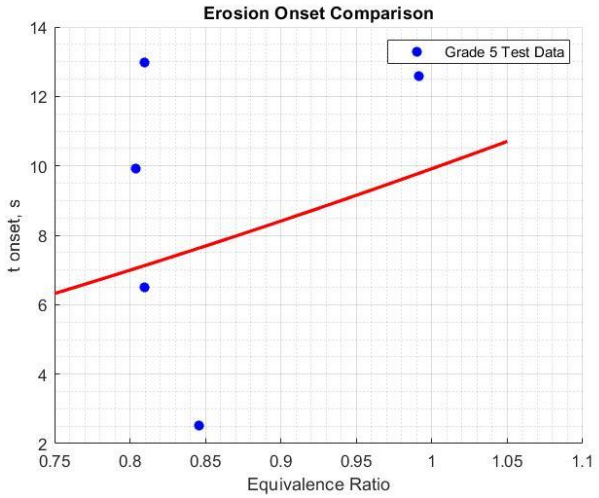

Figure 4.30: Onset Time vs Equivalence Ratios - Grade 5

4.2 Composites

Composite materials offer many advantages compared within the intermediate pressures and nozzle sizes due to their high strength and low density. In this study, carbon phenolic, silica phenolic and C/C materials were tested.

4.2.1 C/C & Carbon Phenolic Test Results

Development processes of C/C are still continued, therefore only one C/C test was performed to compare with carbon phenolic samples. Properties of C/C is given in Table 4.7 & 4.8.

Table 4.6: Properties of C/C

Material	**Bulk Density (g/cm^3)**	**Volume Fraction of Resin**
C/C Composite	1.39	36%

Carbon phenolic samples are prepared by using two different resins by using high pressure press. The same resin type is used for carbon phenolic 1 and carbon phenolic 2. A different type of resin used for carbon phenolic 3. Their specifications are given in Table 4.7.

Table 4.7: Carbon Phenolic Properties

Material	**Bulk Density (g/cm^3)**	**Weight Fraction of Resin**
Carbon Phenolic 1	1.38	35%
Carbon Phenolic 2	1.29	32%
Carbon Phenolic 3	1.29	32%

Table 4.8: Carbon Phenolic and C/C Test Results

Material	t_{burn} (sec)	P_{cavg} (bar)	O/F	$D_{t(i)}$ (mm)	$D_{t(f)}$ (mm)	Erosion Onset (sec)	Erosion Rate (mm/sec)
Carbon Phenolic (1)	11.92	14.37	2.61	7.35	13.25	0.41	0.2562
Carbon Phenolic (2)	11.82	15.8	2.5	7	9.92	0.12	0.1255
Carbon Phenolic (3)	11.92	15.71	2.64	7	10.12	0.16	0.1327
C/C Composite	11.87	15.95	2.68	7	10.75	0.41	0.1636

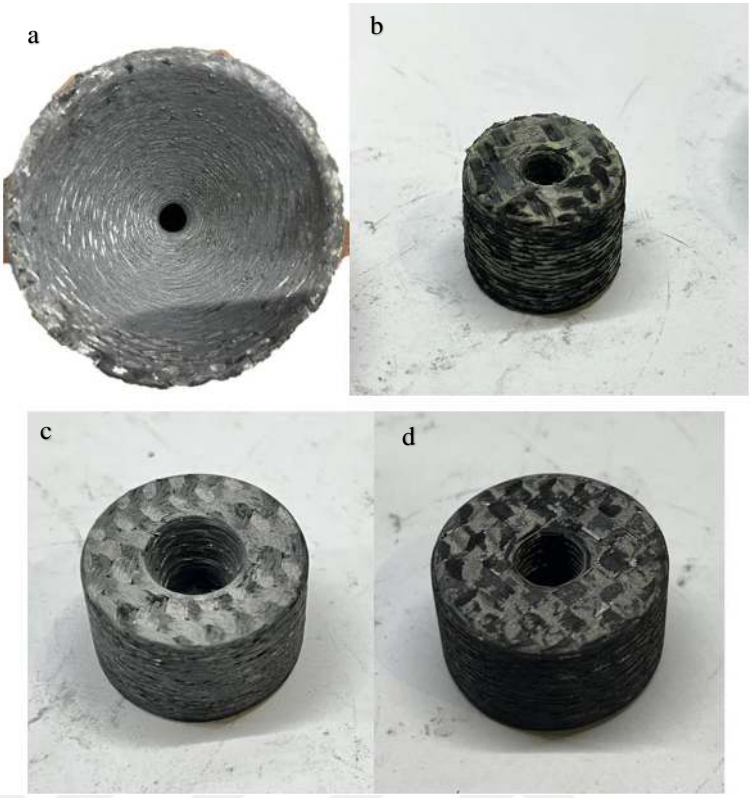

Figure 4.31: a) Carbon Phenolic 1, b) Carbon Phenolic 3, c) Carbon Phenolic 2, d) C/C Composite

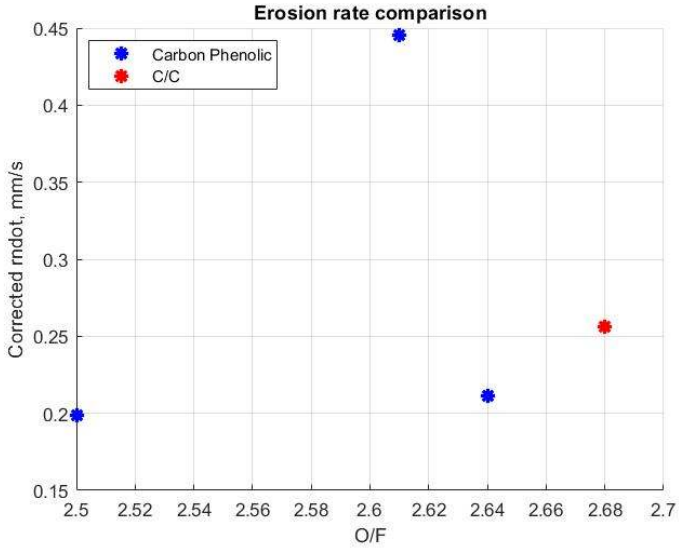

Figure 4.32: Corrected Erosion Rates vs O/F- Carbon Phenolic & C/C

4.2.2 Silica Phenolic Test Results

Silica phenolic samples are prepared by using two different resins and chopped silica fibers. Their specifications are given in Table 4.9.

Table 4.9: Silica Phenolic Nozzle Specifications

Material	**Bulk Density (g/cm^3)**	**Weight Fraction of Resin**
Silica Phenolic 1	1.47	48%
Silica Phenolic 2	1.51	50%

Table 4.10: Silica Phenolic Test Results

Material	t_{burn} (sec)	P_{cavg} (bar)	O/F	$D_{t(i)}$ (mm)	$D_{t(f)}$ (mm)	Erosion Onset (sec)	Erosion Rate (mm/sec)
Silica Phenolic (1)	11.94	10.86	2.72	6.98	13.81	0.43	0.2967
Silica Phenolic (2)	11.93	12.81	2.61	6.98	12.23	0.39	0.2275

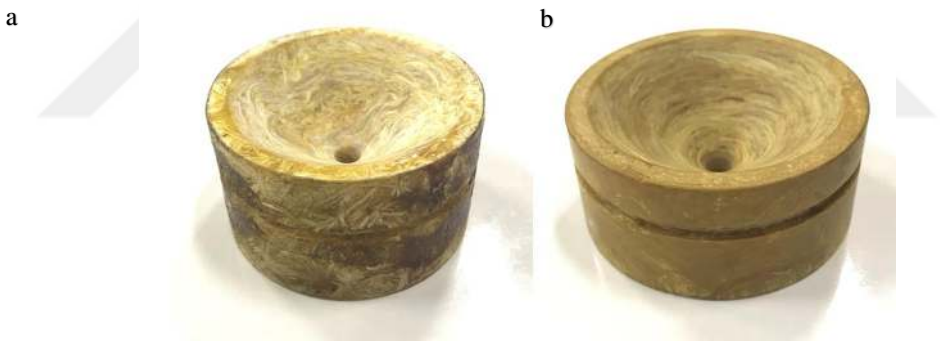

Figure 4.33: a) Silica Phenolic 1, b) Silica Phenolic 2

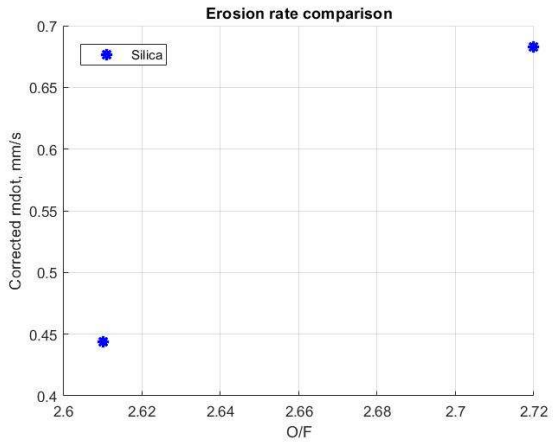

Figure 4.34: Corrected Erosion Rates vs O/F - Silica

4.3 Silicon carbide

4.3.1 SiC Sintering Procedure

In this study, beta phase silicon carbide that has a purity nearly 99% and particle size between 0.1-1 µm is used. Alpha SiC forms at the temperatures above 1700°C however beta phase forms below 1700 °C. Since the sintering temperatures are at above 1700°C and beta phase SiC turn into alpha phase above at this temperature, beta phase SiC is preferred.

There are three major sintering techniques for SiC. In Figure 4.35. Schematic of the sintering techniques are shown. In presureless sintering there is no pressure applied to the specimen while sintering unlike hot isostatic press. In the method of hot isostatic press, pressure and heat are both applied to the specimen. Spark plasma sintering a little bit different from the other techniques. A uniaxial press is used but a voltage is given to the specimen through a die which is generally made of graphite.

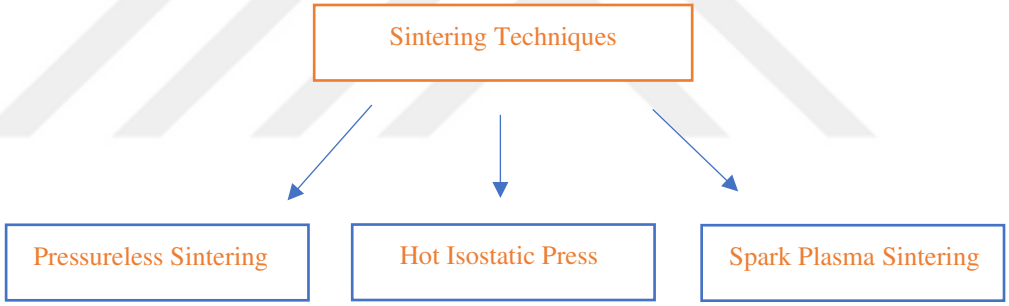

Figure 4.35: Sintering Techniques

German et al. have explained the sintering as ‘‘Sintering is a thermal treatment for bonding particles into a coherent, predominantly solid structure via mass transport events that often occur on the atomic scale. The bonding leads to improved strength and lower system energy’’ [[53], p.4].

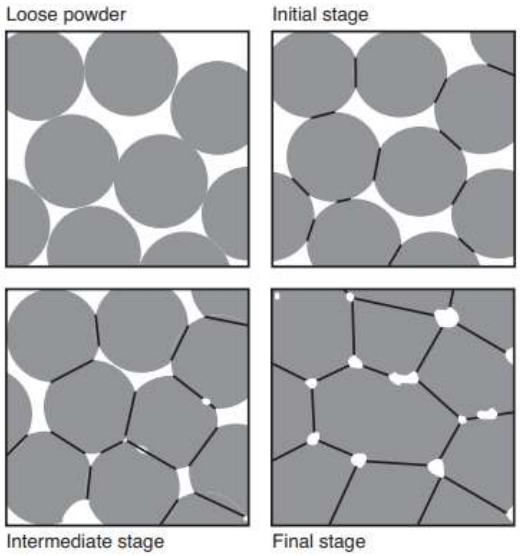

Figure 4.36: Sintering Stages Illustration *[53]*

Wheat et al. stated that the initial stage of sintering is dominated by surface diffusion and occurs at low temperatures [54]. Initial stage of sintering only keeps together the particles, therefore there is no grain growth. The density of the sample is at its green density at this stage. From the processes that were done for this thesis, it is found that the green densities of silicon carbides change between 55-65%. The intermediate stage occurs at high temperatures and dominated by volumetric diffusion. Due to the lattice diffusion from the bulk into the neck region, densification starts. After closing the pores, final stage starts. During this process, most of the closed porosities remove from the sample and the maximum density is achieved.

Sintering process of pure SiC requires high temperatures, therefore additives are used to decrease the sintering temperatures. There are some points to consider while selecting the additives. Reaction between SiC and the additives at the sintering temperature is a critical point due to the decomposition possibility. Additives should be chosen by looking their Gibbs free energy to predict the reactivity. Based on the additive materials, there are two main sintering procedure: solid and liquid phase sintering.

Applying heat to the particles causes bonds and densification between the particles. This process is called as solid-state sintering. The most important thing in the solid-state sintering is giving heat below the melting point of material.

In liquid phase sintering procedure, additives react with the SiO_2 that is on the surface of SiC, and a liquid phase occurs between the SiC powders. There are significant amount of study about LPS of SiC and suitable additives. Kim et al. showed that Al_2O_3, Y_2O_3, MgO, and CaO addition to the SiC gives higher densities [55]. In addition to higher

densities, Kim et al. stated that Y_2O_3 additive is used for heat-resistant SiC, Y_2O_3- Gd_2O_3 are used for an electrically conductive SiC, Y_2O_3- Sc_2O_3 are used for thermal conductive SiC, and Y_2O_3- Sc_2O_3-MgO are used for high strength SiC. Besides, in Reference [56], Raju and Yoon give the effective and ineffective additives for SiC. See Figure 4.37.

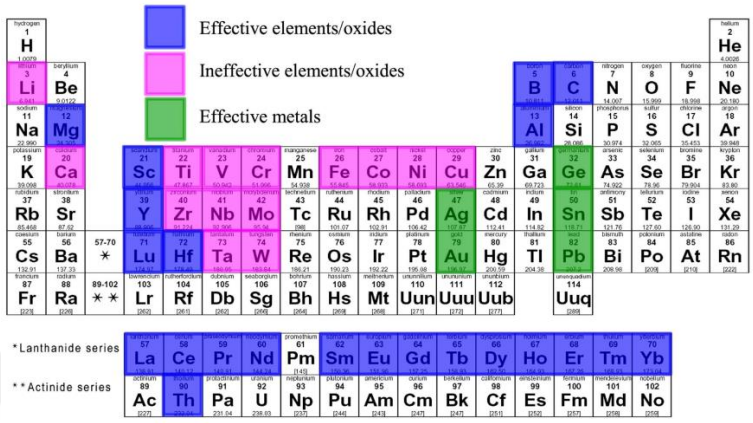

Figure 4.37: Effective and Ineffective Additives for SiC *[56]*

In this study, sintering SiC at lower temperatures was preferred due to low costs and the capabilities of the facility. The aim of this study is achieving the maximum density with a low temperature. Therefore, a formulation was selected from Table 4.10 that is taken from References [55] and [57] which give the maximum density with a low temperature. Gomez et al. give the phase diagram of Al_2O_3/Y_2O_3 and Eutectic point of Al_2O_3/Y_2O_3 is nearly at 1760°C. See Figure 4.38.

Table 4.11: Sintering Additives vs Processing Conditions *[55]*

Additive System	Author	Sintering additives	Processing conditions	Sintered density (%)	Reference
Unary	Kim et al.	12 wt % $Y_3Al_5O_{12}$	1950°C/1 h/Ar	98%	38
Binary	Mulla and Krstic	6 vol % Al_2O_3–Y_2O_3	1850°C/5 min/Ar	97%	39
	Liden et al.	3 wt % Al_2O_3–Y_2O_3	1880°C/4 h/Ar	99.7%	40
	Chen	6 mol % Al_2O_3–Gd_2O_3	1950°C/1 h/Ar	98%	41
	Kim et al.	16.2 wt % Al_2O_3–Y_2O_3	1950°C/3 h/Ar	97.3%	21
	She and Ueno	10 wt % Al_2O_3–Y_2O_3	1950°C/1 h/Ar	98%	42
	Winn and Clegg	3 wt % Al_2O_3–Y_2O_3	1950°C/4 h/Ar	98%	43
	Baud et al.	17 wt % Al_2O_3–$Y_3Al_5O_{12}$	1950°C/3 h/Ar	98%	44
	Magnani et al.	10 wt % Al_2O_3–Y_2O_3	1875°C/0.5 h/Ar	97.1%	22
	Liang et al.	7 wt % Al_2O_3–CeO_2	1840°C/1 h/Ar	99.1%	45
	Liang et al.	7 wt % Al_2O_3–Er_2O_3	1880°C/1 h/Ar	98%	46
	Liang et al.	6 wt % Al_2O_3–Y_2O_3	1920°C/1 h/Ar	98.5%	47
	Ribeiro et al.	14.62 wt % Al_2O_3–Dy_2O_3	1800°C/1 h/Ar	92.3%	25
	Ribeiro et al.	15.58 wt % Al_2O_3–Yb_2O_3	1800°C/1 h/Ar	92.0%	25
	Santos and Ribeiro	10 vol % AlN–Dy_2O_3	1950°C/2 h/Ar	98.6%	26
	Santos and Ribeiro	10 vol % AlN–Yb_2O_3	2000°C/2 h/Ar	99.5%	26
Ternary	Goldstein et al.	9 vol % Al_2O_3–Y_2O_3–C	1950°C/1.5 h/Ar	98.5%	48
	Marchi et al.	10 mol % Al_2O_3–Y_2O_3–SiO_2	1950°C/1 h/Ar	95%	49
	Gubernat et al.	10 wt % Al_2O_3–Y_2O_3–MgO	1950°C/2 h/Ar	96%	27
	Liang et al.	12 wt % Al_2O_3–Y_2O_3–TiO_2	1920°C/0.5 h/Ar	99.2%	31
	Eom et al.	3 vol % Al_2O_3–Y_2O_3–AlN	1900°C/1 h/Ar	99.4%	28
	Eom et al.	9 wt % Al_2O_3–Y_2O_3–CaO	1850°C/2 h/Ar	99%	29
	Cho et al.	6.5 vol % Y_2O_3–Sc_2O_3–AlN	1950°C/6 h/N_2	98.6%	30
	Kim et al.	3 vol % Al_2O_3–Y_2O_3–AlN	1900°C/1 h/Ar	97.0%	50
Quaternary	Seo et al.	9.07 wt % Al_2O_3–Y_2O_3–SrO–CaO	1800°C/2 h/Ar	95.2%	32
	Seo et al.	9.07 wt % Al_2O_3–Y_2O_3–SrO–CaO	1900°C/2 h/Ar	96.7%	32
	Kim and Kim	9 wt % Al_2O_3–Y_2O_3–MgO–CaO	1800°C/2 h/Ar	98.8%	This study

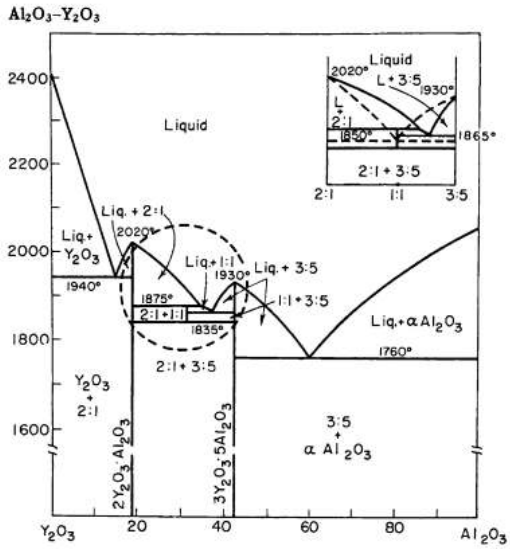

Figure 4.38: Phase Diagram of Al2O3/Y2O3

Gomez et al. stated that, after a point of sintering temperature, density decreases. Therefore, the optimum sintering temperature for the formulation should be found. He gives density vs temperatures graphs of different formulations in his study. See Figure 4.39 & 4.40 and Table 4.9.

Table 4.12: Nomenclature ad Chemical Composition of Samples at Ref. *[57]*

Label	Base powder	C	Y_2O_3	Al_2O_3	SiO_2
β460	β	–	4	6	–
β640		–	6	4	–
β605		–	6	–	5
β625		–	6	2	5
α460	α	–	4	6	–
αC460		4	4	6	–
αC605		3	6	–	5
βα460	β + 10%α	–	4	6	–
βαC460		4	4	6	–
βα230		–	2	3	–
βαC230		4	2	3	–
βα640		–	6	4	–
βαC640		4	6	4	–
βα320		–	3	2	–
βαC320		4	3	2	–
βα605		–	6	–	5
βα625		–	6	2	5

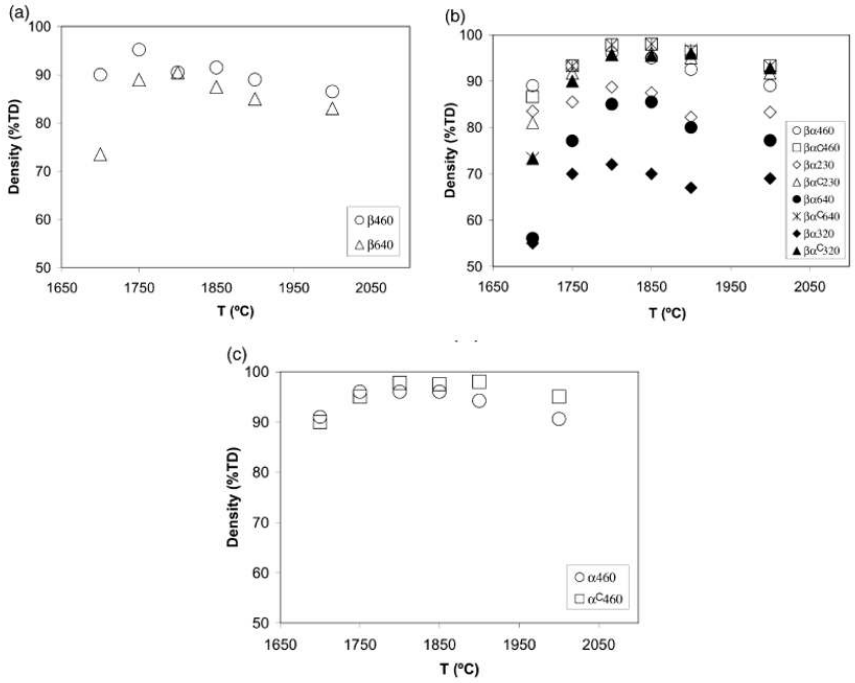

Figure 4.39: Density vs Temperature of Various Formulations *[57]*

Since βαC460 formulation gives nearly the maximum densities at low temperatures, this formulation from Reference [57] was selected for this study. 10 % of the mixture compose of additives with 4% Y_2O_3 and 6% Al_2O_3. In addition to this, 4% carbon was added to the SiC that has 99% purity. Phenolic resin is used as carbon source and binder.

Preparation of powder mixture is a time-consuming process. First of all, powder mixture is mixed by using IPA and ball mill nearly six hours. After ball milling process, to evaporate the IPA from mixture, the mixture is waited on a stirrer nearly at 80 °C for a day. After the evaporation of the solvent, the mixture is dried in a vacuum furnace nearly 2 hours. Then, the mixture is sieved by using a sieving machine with a 80 μm mesh. Prepared powder mixture is pressed by using a uniaxial press with a pressure of 500 bar. Samples are in 30 mm in diameter and nearly 20 mm in thickness. Green compact sample densities are nearly 55-60% at this stage. In addition to uni-axial pressing, isostatic press is also required. Cold isostatic press is used in this study due to its low cost. Specimens are covered with a film layer that transmits the pressure to the specimen and then the specimens are left into the oil. 2500 bar pressure is applied to the samples. After all of these stages, debinding process is applied to the samples for pyrolysing the phenolic resin. Debinding process is done at 800 °C for 1 hour under N_2 atmosphere. Machining process is done after the debinding process, because samples are more compact and brittle at this

stage and this situation eases the machining process. Finally, the samples are heated with a 10°C/min rate to 1500 °C. Since the reaction Gibbs free energy of SiO_2 and C turns into negative at 1500 °C, samples stay at this temperature for 30 minutes. Then, samples are heated with a 10°C/min rate to required sintering temperature, which is generally 1900 °C for this study, under the Argon atmosphere for 1 hour in a graphite crucible. This process is similar to the process that Malinge et al. uses [58].

In Figure 4.39, SiC sample after uniaxial, isostatic&debinding&machining, and sintering is shown. In this study, maximum 98 % density is achieved. Samples that are used in the test have densities between 88-98%.

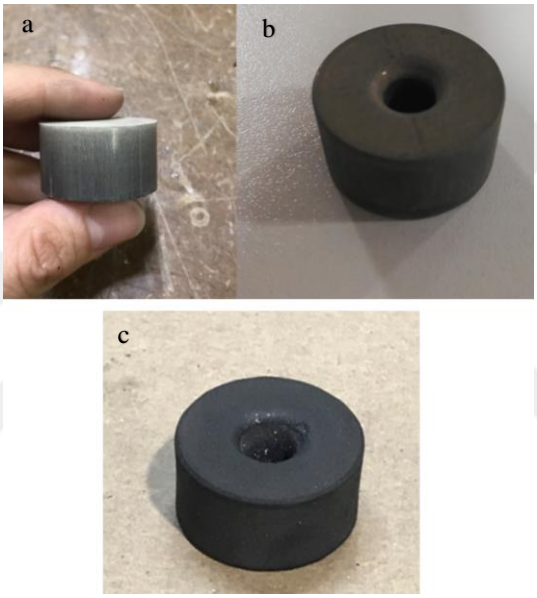

Figure 4.40: a) SiC after Uniaxial Press, b) SiC after Debinding and Machining, c) SiC after Sintering

4.3.2 SiC Test Results

In Figure 4.40, SiC insert for the nozzle can be seen. SiC sample is inserted in two pieces of graphites.

Figure 4.41: SiC Nozzle Insert

Table 4.13: Silicon Carbide Test Results

Material	t_{burn} (sec)	P_{cavg} (bar)	O/F	$D_{t(i)}$ (mm)	$D_{t(f)}$ (mm)	Erosion Onset (sec)	Erosion Rate (mm/sec)
SiC 1_4	11.8	26.4	2.77	6.5	7.635	5.40	0.0887
SiC 2_3	11.89	23.77	2.52	6.5	7.09	8.99	0.1017
SiC 3_1.3	11.87	27.18	2.88	6.83	7.66	5.86	0.0691
SiC 4_2	11.89	28.9	3.03	6.8	8.11	4.89	0.1407
SiC 5	14.92	22.93	2.58	6.85	8.26	4.98	0.0704

4.4 Metals

Due to their high strength metals can be preferred as nozzle materials although their cost effectiveness and high density. Since there is a problem about supplying the molybdenum and tungsten, numbers of the tests are limited for this study. In the future works more tests will be performed.

4.4.1 Molybdenum

Molybdenum which has a purity nearly 99.9% is used in the tests. Since molybdenum has high cost and there is a problem about supply, only two tests performed. Molybdenum is used as an insert to decrease the cost.

Table 4.14: Molybdenum Test Results *[13]*

Material	t_{burn} (sec)	P_{cavg} (bar)	O/F	$D_{t(i)}$ (mm)	$D_{t(f)}$ (mm)	Erosion Onset (sec)	Erosion Rate (mm/sec)
Molybdenum 1	14.93	24	2.92	6.99	8.38	8.53	0.1082
Molybdenum 2	15.88	24	2.82	6.99	8.19	10.51	0.1117

Figure 4.42: Molybdenum Nozzle Insert

4.4.2 Tungsten

Tungsten which has a purity nearly 92.5% is used in the tests. There are 5.25 % Ni and 2.25% Fe additives in this alloy. Since tungsten has high cost and there is a problem about supplying, only 4 tests performed. In one of the tests, graphite around the tungsten cracked and tungsten insert hurtled during the purge. Besides, in another test, tungsten melted and half of it hurtled. Therefore, in these two tests measurements of nozzle failed. As a result, only two test results were investigated.

Table 4.15: Tungsten Test Results

Material	t_{burn} (sec)	P_{cavg} (bar)	O/F	$D_{t(i)}$ (mm)	$D_{t(f)}$ (mm)	Erosion Onset (sec)	Erosion Rate (mm/sec)
Tungsten 1	11.41	25.95	2.2	7.5	8.5	3.95	0.067
Tungsten 2	11.88	22.83	2.69	7.0	7.14	9.81	0.0338

Figure 4.43: Tungsten Nozzle Insert

Chapter 5:
DISCUSSION

Seven different materials were tested, and their results were given in Chapter 4. First of all, five different graphite types were tested, and it is obvious that there is a direct proportion between the grain size and erosion rates. For graphite types, grain size, thermal conductivity, porosity, ash content and density are very important parameters and all of them are interrelated. If a graphite has low grain size, sintering of this type or graphite should be better. Therefore, its density will also be higher. Dense graphite has low porosity and should conduct the heat better. Thus, its thermal conductivity will also be high. In erosion characterization test that were done in this study, selection of graphite types was done based on the grain size and thermal conductivity. If a material has lower grain size, this will cause smaller particles to break off during the reactions. This is because erosion rates are smaller in the graphite that has lower grain sizes. In addition to this, thermal conductivity has an effect on erosion, because a material with a high thermal conductivity transmits the heat quickly and the surface will remain colder. Since reactions at the nozzle surface starts at high temperatures depending on the reaction, keeping the surface cold will retard the reactions. Among the types in this study, Grade 5 has the smallest grain size and highest thermal conductivity. As expected for the reasons explained above, Grade 5 performed the best performance among all graphite types. There is an example of eroded nozzle throat of Grade 1 in Figure 5.1. Besides, in Figure 5.2, erosion rates of all graphite types are shown.

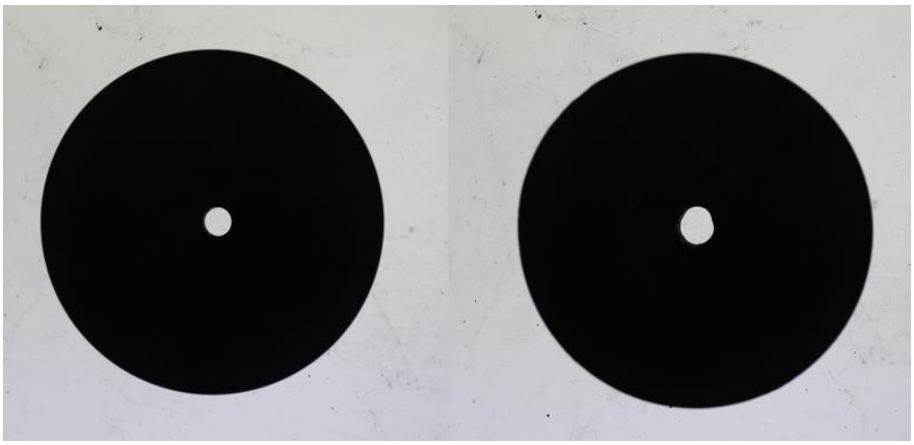

Figure 5.1: Grade 1 Nozzle Erosion after 12 Seconds Burn Time *[13]*

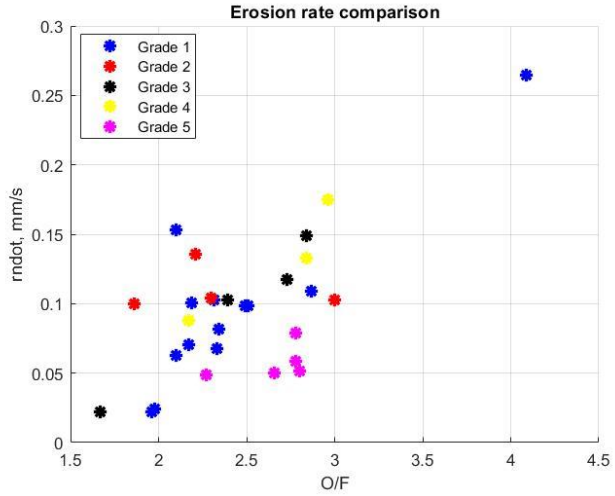

Figure 5.2: Erosion Rates of all Graphite Grades vs O/F

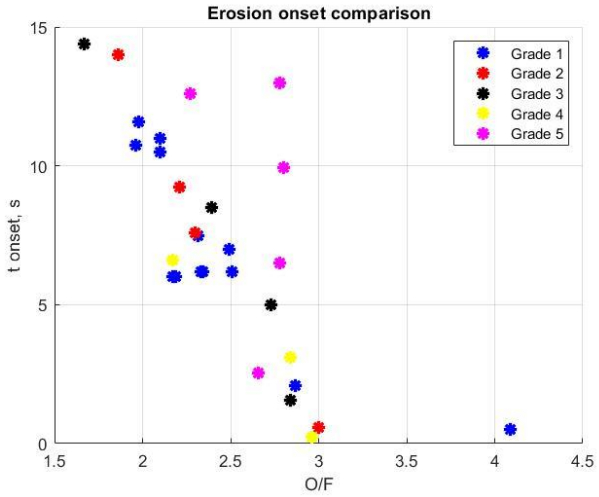

Figure 5.3: Onset Times of all Graphite Grades vs O/F

Secondly, composites such as C/C, carbon phenolic, and silica phenolic were tested. Their production were done in DeltaV Space Technologies and their development process is still continue. Carbon fiber fabric were used to prepare C/C composites and carbon phenolic samples. Two different types of resins were used in carbon phenolic samples and their performances were investigated. Besides, C/C composite was prepared by doing three polymer infiltration and pyrolysis (PIP) cycles. If pyrolysis cycles are increased, samples that have higher densities can be obtained. Besides, carbon-based composites will perform close to graphite if they have very low porosities. They are much more eroded than graphite because their porosities are higher. If C/C composites are prepared at high densities, that is expected to have lower erosion rates due to low porosities of

samples. However, in this study the density of C/C was not as high as it should have been. Besides, only one test could be done. When the test results are examined, it is seen that carbon-based composite materials give close results to each other. Therefore, it is planned to add tests at different resin and O/F ratios in future studies. However, as mentioned above, composites are not very suitable materials for hybrid and liquid rocket nozzle throats due to high oxidizing agents in the combustion products. They can be preferred in extension areas of HRMs and LREs where temperature and pressure are lower. Composite materials can be suitable for the solid rocket motors since they have high strength and are resistant to mechanical erosion.

Figure 5.4: Carbon Phenolic1 Throat Erosion after 12 sec Burn

Figure 5.5: C/C Throat Erosion after 12 sec Burn Time

Silica phenolic samples were prepared using chopped silica fiber using two different resins. The results of the resin used in sample 1 were expected to be worse than in sample 2. Test results were as expected and the second sample showed better results in terms of erosion. It has been determined that the erosion rates of silica samples are higher than carbon composites because silica melts above 1700°C and its mechanical strength also decreases.

Figure 5.6: Silica Phenolic Nozzle 1 after 12 sec Burn

Figure 5.7:Silica Phenolic Nozzle 2 after 12 sec Burn

Tungsten can be preferred in HRMs due to its high melting temperature, but its weight is a disadvantage for it. One of the most important disadvantages is its fragility. It has already been observed that it is broken in one of the tests. In addition to this, since it is a metal, its probability of oxidation is higher, so they may not be very suitable for environments which contain high amount of oxidizing agents. For these reasons, it can be preferred at HRMs that operates at low O/F ratios. These reasons are also valid for molybdenum. Although its density is lower than tungsten, it is still heavier than composites and graphite. Another disadvantage is that molybdenum has a lower oxidation

temperature than tungsten. The effect of this was also seen in the test results, and the molybdenum nozzle throat was further eroded. In Figure 5.6, eroded tungsten nozzle inserts and in Figure 5.7 eroded molybdenum is shown. Normally, tungsten would be expected to perform better performance than the tests in this study, but since its purity is nearly 93%, it is thought to be more eroded due to impurities in its content.

Figure 5.8: Tungsten Nozzle after 12 sec Burn at 2.7 O/F

Figure 5.9: Molybdenum Nozzle Insert after 12 sec Burn

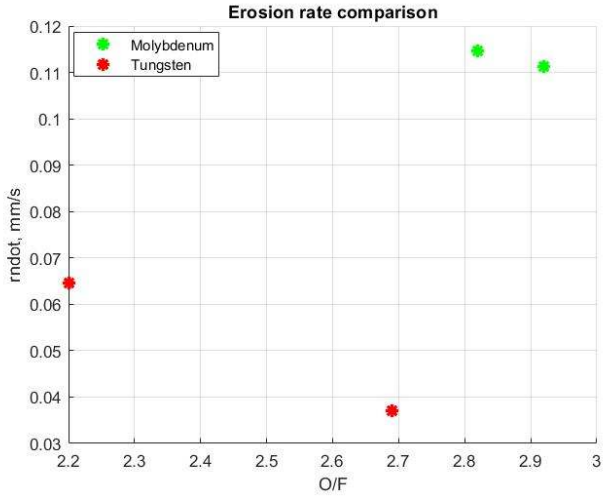

Figure 5.10: Erosion Rate Comparison of Mo & W

Silicon carbide is one of the important materials that should be developed for use in hybrid rocket motors due to its high strength. There are few studies on the use of silicon carbide in hybrid rocket motors [59] [60]. In both studies, it was observed that the nozzle was broken. In reference [60], silicon carbide is reinforced with metal fibers to prevent cracks. In this thesis study, different densities of silicon carbides with the same formulation were tested. Early in the research, there was a problem with the furnace and the sintering temperatures were measured incorrectly. Therefore, the samples in that process were sintered at a higher temperature than expected. It was stated that in the reference [58] that when the temperature rises a lot, the density drops, and it did. A sample with a density of 88% was obtained from this process. Although three of the other four samples were sintered at 1900 °C, there were slight difference in their densities. Densities of the tested samples are given in Table 5.1.

Table 5.1: Silicon Carbide Sintering Temperature & Density

Sample	Sintering Temperature	Density
SiC1_4	1900 °C	98%
SiC2_3	1900 °C	97%
SiC3_1.3	1800 °C	95%
SiC4_2	1900 °C	96%
SiC5	Above 2300 °C	88%

According to the results in the tests, although the density of the first four samples was higher, they performed worse than they should have been. The reason for this was investigated and the following reasons were found. First, the sample named SiC5 was prepared, and during this time, the temperature could not be measured correctly due to the problem arising from the furnace and it is thought that it exceeded 2300 °C. Also, due to the alumina and carbon in the formulation, alumina and carbon particles in the sample form Al_4C_3 during the sintering procedure. Above 2300 °C, this Al_4C_3 evaporates, Therefore, it is thought that the furnace is contaminated with impurities. As the other samples prepared later waited, dust formed on their surfaces. In addition, droplet-shaped samples were also seen in the crucible of the samples taken out of the furnace. When these powders were examined with EDX and SEM, it was understood that they were Al_4C_3. In Figure 5.12, dusty surface of the SiC and the metal droplets in the crucible are shown. Soto et al. touched on this issue in their article. They observed Al-C-Si mixed

carbides on the surface of the material. Besides, in XRD diffraction patterns they observed Al_4C_3 and $Al_4C_7Si_4$ [61]. In Figure 5.11, XRD patterns in Reference [61] can be seen.

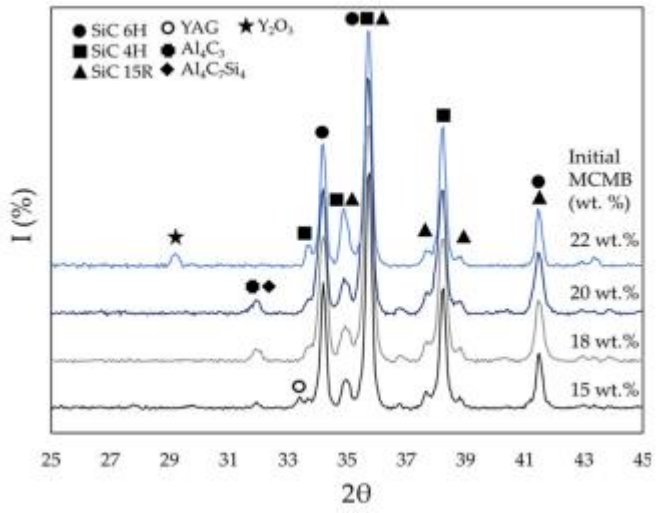

Figure 5.11: XRD Diffraction Patterns of SiC Surface

Figure 5.12:Dusty Surface on SiC and Droplets on Crucible

EDX analysis of dusty surface of the SiC and droplets on the crucible are given in Figure 5.13&5.14&5.15&5.16. It is clearly seen that Al and C amounts are high. In addition, hydroxyl crystals on the surface are seen in SEM photos in Figure 5.17&5.18.

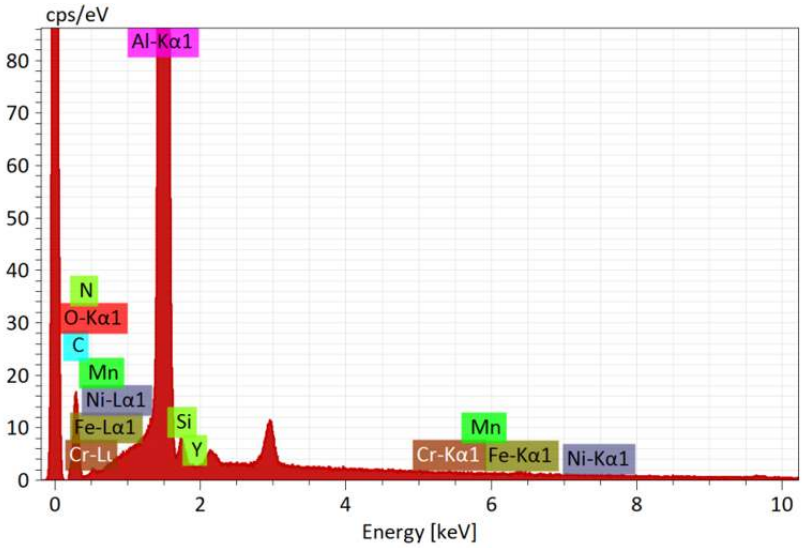

Figure 5.13: EDX Analysis of Dusty Surface

AN05P176 561

Element	At. No.	Netto	Mass [%]	Mass Norm. [%]	Atom [%]	abs. error [%] (1 sigma)	rel. error [%] (1 sigma)
C	6	21639	27.39	30.54	49.01	3.51	12.81
Al	13	1385063	59.30	66.10	47.22	2.85	4.81
N	7	1145	1.63	1.81	2.50	0.38	23.36
O	8	1072	0.51	0.57	0.69	0.14	27.11
Si	14	8704	0.65	0.72	0.50	0.05	8.38
Fe	26	961	0.15	0.17	0.06	0.03	20.83
Cr	24	247	0.03	0.03	0.01	0.00	7.34
Mn	25	210	0.03	0.03	0.01	0.00	7.84
Ni	28	82	0.02	0.02	0.01	0.00	11.86
Y	39	0	0.00	0.00	0.00	0.00	1.94
		Sum	**89.71**	**100.00**	**100.00**		

Figure 5.14: EDX Analysis Results of Dusty Surface

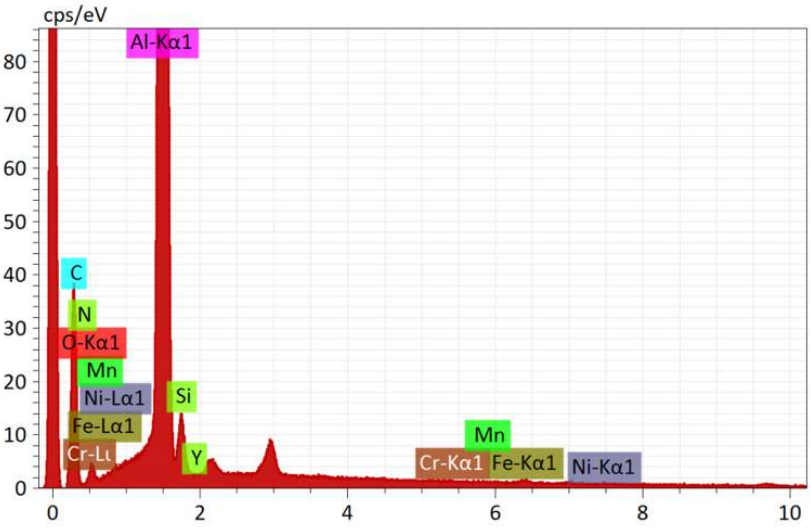

Figure 5.15: EDX Analysis of Droplets

AN05P176 560

Element	At. No.	Netto	Mass [%]	Mass Norm. [%]	Atom [%]	abs. error [%] (1 sigma)	rel. error [%] (1 sigma)
C	6	46421	52.91	45.35	63.19	6.30	11.90
Al	13	1067102	55.26	47.36	29.38	2.66	4.82
N	7	2296	4.19	3.59	4.29	0.79	18.95
O	8	4157	2.64	2.26	2.37	0.45	17.15
Si	14	18381	1.37	1.17	0.70	0.08	6.21
Fe	26	1223	0.21	0.18	0.05	0.03	15.87
Ni	28	283	0.06	0.05	0.02	0.03	46.80
Cr	24	165	0.02	0.02	0.01	0.00	8.71
Mn	25	72	0.01	0.01	0.00	0.00	12.60
Y	39	0	0.00	0.00	0.00	0.00	1.94
		Sum	**116.67**	**100.00**	**100.00**		

Figure 5.16: EDX Analysis Results of Droplets

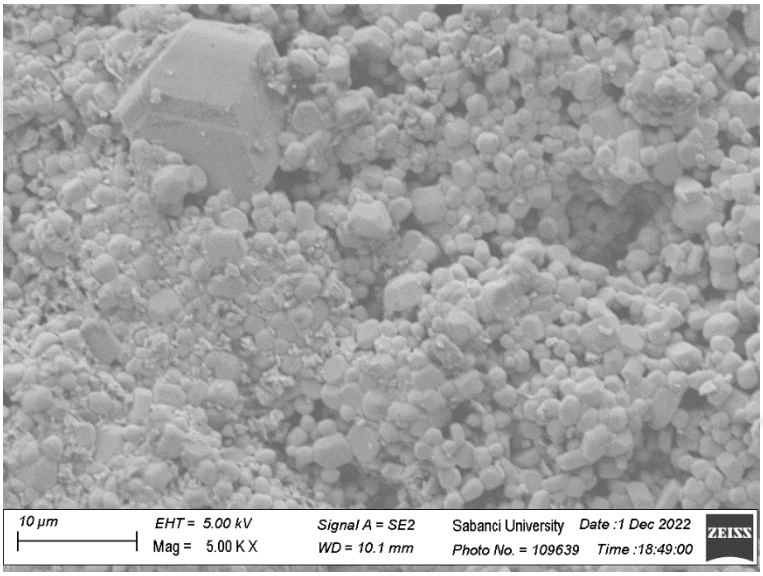

Figure 5.17: SEM Images of Dusty Surface

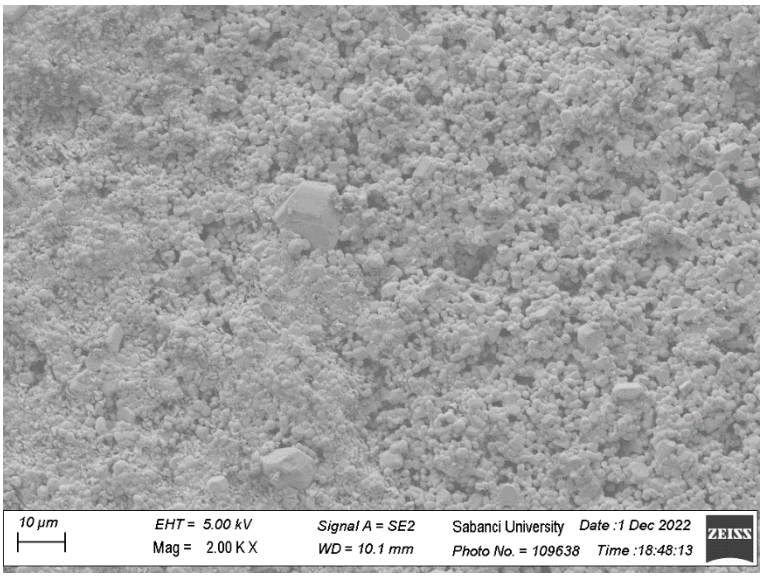

Figure 5.18: SEM Images of Dusty Surface

SiC 5 was compared with the Grade 1 and Grade 5 graphite since it is thought that the Grade 1 and 5 are the best graphite. See Figure 5.19. As a result of this comparison, it gave better results when tested under the same conditions as graphite, despite having low density. The reason for this thought to be the absence of Al_4C_3 formation on the surface of the sample.

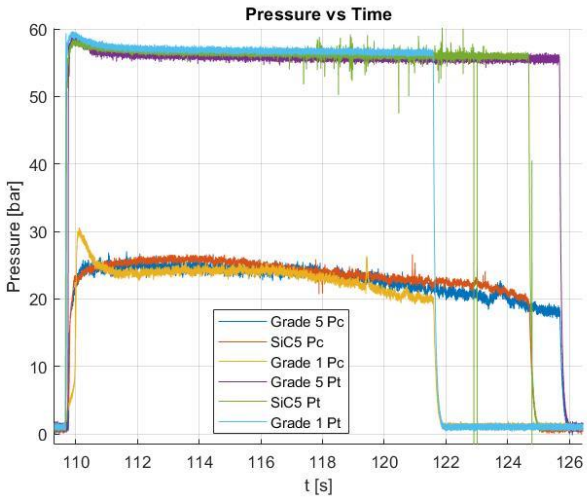

Figure 5.19: SiC & Grade 1 & Grade 5 Comparison

Another advantage of SiC in erosion is thought to be the silica layer that melts and covers the surface. This silica layer covering the surface protects the surface and delay the onset of erosion. This layer is clearly visible on the nozzle surface after the tests. Figure 5.20 shows the onset times of graphites and SiC. Figure 5.21, silica layer on the nozzle surface can clearly be seen.

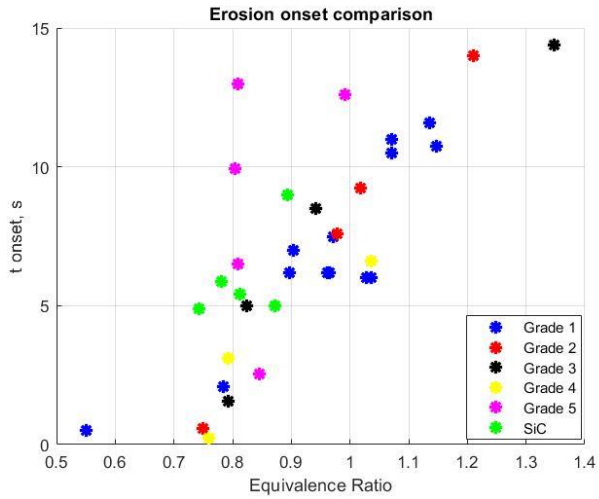

Figure 5.20: Erosion Onset Times of Graphites & SiC

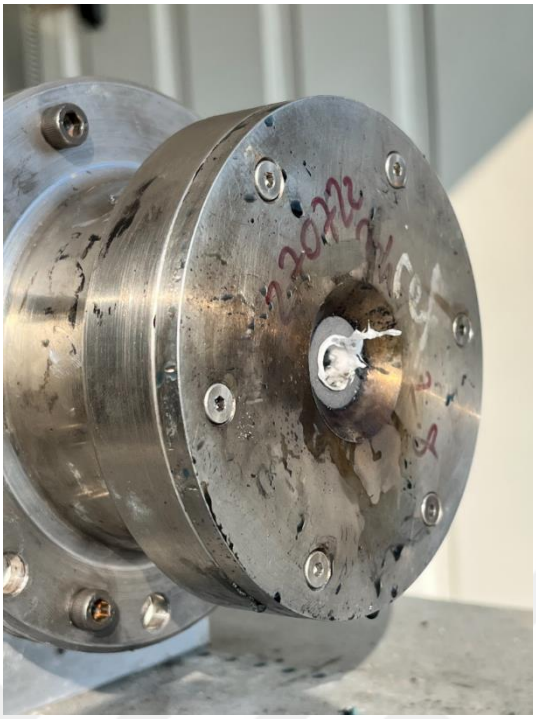

Figure 5.21: Silica Layer on the Inner Surface of Nozzle

After the test, it was observed that the SiC nozzle inserts cracked. After the samples are snterd, they cannot be machined due to their hardness and each sample shrinks at different rates. There is a difference in the shrinkage ratio between the surfaces of the samples that touch the crucibles and the surfaces that do not. For this reason, the samples cannot be machined in sensitive tolerances and cannot be made exactly in accordance with the dimensions of the graphite parts outside. It is thought that this is the reason for their cracking and formulation and production developments are continuing to prevent them from cracking. In Figure 5.22, cracks on the SiC after the test are shown.

Figure 5.22: Cracks on the Surface of SiC After the Test

.

Chapter 6:
CONCLUSION

In conclusion, among five tested different graphite, Grade 5 performed the best performance. It is obvious that there is an inverse proportion between the grain size and erosion rates. Not only the grain size affects the erosion rates, but also density, porosity, thermal conductivity, and ash content are important parameters for graphite nozzle erosion rates.

According to the test results of composite materials, it has been seen that they are not very suitable for HRM and LRE throats due to their high erosion rates. However, it may be particularly suitable for SRM nozzles since they require mechanical strength due to the mechanical erosion in SRM nozzles. In addition, silica phenolic, carbon phenolic, and seramic matrix composites can be used in the nozzle extensions of HRMs. Because the temperature and pressure tend to decrease towards the outlet in the nozzle extension part.

Among the metals tested, it was seen that the material that gave the best results was tungsten. Molybdenum erodes more quickly due to its low oxidation temperature. The disadvantages of tungsten are that it cannot be used in repeated applications due to the its brittleness, difficulty in its machinability, and its weight. In addition to this, materials with high purity will reduce erosion rates. Depending on the applications, preference can be made between other tested materials and metals.

One of the other reasons affecting erosion apart from the material is working at low O/F and pressure. Due to the high O/F ratios, high amount of free oxygen is released with the combustion products and these oxygen atoms react with the nozzle material at high temperatures and cause erosion. In addition, it is expected that the amount of erosion will increase as the increase in chamber pressure since it increases the heat fluxes on the nozzle surface. Therefore, reducing the O/F ratio and working at low chamber pressures may be an option to reduce erosion.

Another option to reduce erosion is to change fuel formulation. Karakas et al. examined the erosion rates using different metal additives and determined the most suitable additive as aluminum in terms of cost, availability, and performance. The aluminum in the fuel reacts with the free oxygens in the environment, thus, reducing the

amount of oxygen it reduces the erosion. Besides, since aluminum reduces the optimum O/F ratio, working at a low O/F ratio also reduces erosion rates as mentioned above.

In this thesis study, the effect of the nozzle throat length on erosion was also examined and it was observed that the erosion decreased as the length increased. However, it has been observed that erosion rates begin to increase when the length to diameter ratio exceeds almost 1. In addition to this, more tests are needed to create a good data set, and this will be one of the future studies. In addition, in the following study, it is planned to look at the effect of length in different size of nozzles at various O/F ratios, because effect of L/D can change in large scale motors.

The material that gives the best results among the SiC tests is the sample that does not have aluminum carbide dust on its surface. This is because aluminum carbide is hydrophobic and, in this case, the water in the combustion products reacts with the material. In this context, new formulation developments and optimization studies continue.

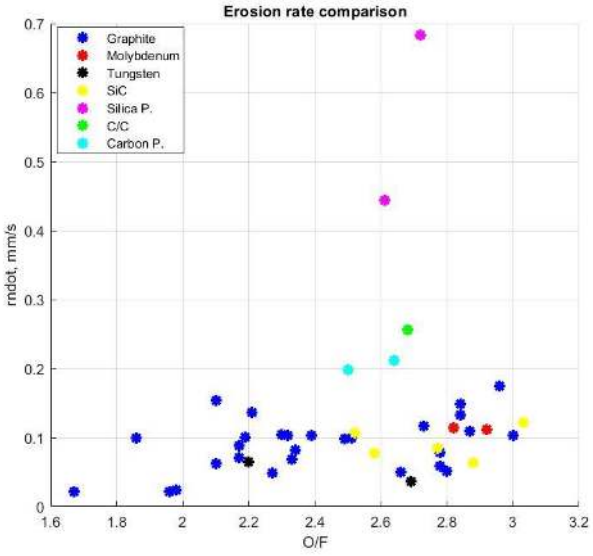

Figure 6.1: Corrected Erosion Rates vs O/F of All Tested Material

As a result, the material that gives the best results among the tested material is Grade 5. However, since SiC gives results close to Grade 5 if it sintered well, it has been seen that SiC can also be used in rocket nozzles. Considering all these inferences, it can be said that SiC is a promising material.

One of the future works will be SiC formulation and sintering process development for HRM nozzle throats. Secondly, niobium, a metal different from those used in this

thesis, will be tested and and further tests will be carried out to compare the erosion rates with molybdenum and tungsten. Finally, more detailed studies will be conducted on the effect of the length of the nozzle throat on erosion and it is planned to support the tests with analysis.

BIBLIOGRAPHY

[1] E. Papadopoulus, "Heron of Alexandria (c. 10-85 AD)," in *Distinguished Figures in Mechanism and Machine Science*, Dordrecht, Springer, 2007, pp. 217-245.

[2] NASA, "nasa.gov," [Online]. Available: https://www.nasa.gov/sites/default/files/atoms/files/rockets-guide-20-history.pdf. [Accessed 24 December 2022].

[3] Anon., "Blogs.esa.int," ESA, 14 10 2012. [Online]. Available: https://blogs.esa.int/rocketscience/2012/10/14/a-man-and-an-equation/. [Accessed 24 December 2022].

[4] V. Badescu and M. Macdonald, The International Handbook of Space Technology, New York: Springer, 2014.

[5] H. Oberth, The Rocket into Planetary Space, Munich: Verlag R. Oldenbourg, 1923.

[6] NASA, "nasa.gov," [Online]. Available: https://www.nasa.gov/centers/goddard/about/history/dr_goddard.html. [Accessed 24 December 2022].

[7] Wikipedia, «en.wikipedia.org,» [Çevrimiçi]. Available: https://en.wikipedia.org/wiki/V-2_rocket. [Erişildi: 28 December 2022].

[8] ESA, "esa.int," [Online]. Available: https://www.esa.int/About_Us/ESA_history/50_years_of_humans_in_space/Sergei_Korolev_Father_of_the_Soviet_Union_s_success_in_space. [Accessed 24 December 2022].

[9] G. P. Sutton, Rocket Propulsion Elements, Delhi: John Wiley & Sons, 2013.

[10] P. Narsai, *Ph.D Dissertation, 'Nozzle Erosion in Hybrid Rocket Motors',* Stanford, CA: Department of Aeronautics and Astornautics, Stanford University, 2016.

[11] M. A. Karabeyoglu, "AA284a Advanced Rocket Propulsion_Lecture1," Stanford University, 2013.

[12] NASA, «grc.nasa.org,» [Çevrimiçi]. Available: https://www.grc.nasa.gov/www/k-12/airplane/lrockth.html. [Erişildi: 28 12 2022].

[13] B. Kahraman, H. Karakas, B. N. Eren and M. A. Karabeyoglu, "Erosion Rate Investigation of Various Nozzle Materials in Hybrid Rcoket Motors," in *AIAA Propulsion and Energy*, 2020.

[14] M. A. Karabeyoglu, «AA284a Advanced Rocket Propulsion_Lecture5,» Stanford University, 2019.

[15] M. A. Karabeyoğlu, D. Altman and B. J. Cantwell, "'Combustion of Liquefying Hybrid Propellants: Part1, General Theory'," *Journal of Propulsion and Power,* vol. 18, no. 3, May-June 2002.

[16] M. A. Karabeyoglu , B. Cantwell and J. Stevens, "Evaluation of Homologous Series of Normal Alkanes as Hybrid Rocket Fuels," in *41th Joint Propulsion Conference*, July 2005.

[17] M. A. Karabeyoğlu, B. J. Cantwell and G. Zilliac, "Development of Scalable Space-time Averaged Regression Rate Expressions for Hybrid Rockets'," *Journal of Propulsion and Power,* vol. 23, no. 4, July-August 2007.

[18] L. Meyer, "The Surface Reaction of Graphite With Oxygen Carbon Dioxide and Water Vapour at Low Pressures," *Transactions of the Faraday Society,* vol. 34, no. 1056, pp. 1056-1061, 1938.

[19] R. F. Strickland-Constable, "The Interaction Oxygen and Carbon Filaments at High Temperatures," *Transactions of the Faraday Society,* vol. 40, pp. 333-343, 1944.

[20] L. T. Kamps, *Ph.D Dissertation, 'Mechanisms of Graphite Nozzle Erosion in Hybrid Rockets',* Hokkaido University, September, 2019.

[21] G. Sutton ve O. Biblarz, %1 içinde *Rocket Propulsion Elements*, New York, Wiley, 2001, pp. 592-620.

[22] L. T. Kamps, H. Shota, K. Sakurai, T. Viscor, S. Yuji, R. Guan, H. Isochi, N. Adachi, I. Mitsinori and H. Nagata, "Investigation of Graphite Nozzle Erosion in Hybrid Rocket Motors Using O2/C2H4," in *AIAA Propulsion and Energy*, Cincinnati, July9-11, 2018.

[23] D. Bianchi, F. Nasuti and M. Onofri, "Thermochemical Erosion Analysis for Ghraphite&Carbon-Carbon Rocket Nozzles," *Journal of Propulsion and Power,* vol. 7, no. 2, 2011.

[24] D. Bianchi and F. Nasuti, "Numerical Analysis of Nozzle Material Thermochemical Erosion in Hybrid Rocket Engines," in *48th AIAA/ASME/SAE/ASEE Joint Propulsion Conference & Exhibit*, Atlanta, 30 July-1 August 2012.

[25] S. A. Whitmore, R. Bubb, T. J. Gardner, K. P. Lloyd and J. C. Stephens, "Pyrolytic Graphite and Boron Nitride as Low-Erosion Nozzle Materials for Long-Duration Hybrid Rocket Testing," in *AIAA Propulsion and Energy* , Virtual Event, August24-28, 2020.

[26] H. Karakas, O. Kara, B. Kahraman, B. N. Eren, I. Ozkol ve M. A. Karabeyoglu, «Influence of Micro-Aluminum Addition to Paraffin-Based Fuels on Graphite Nozzle Erosion Rate,» %1 içinde *AIAA Propulsion and Energy*, August, 2020.

[27] H. Karakas, O. Kara, I. Ozkol and M. A. Karabeyoglu, "Performance Enhancing Additives for Hybrid Rockets," in *AIAA Propulsion and Energy*, 2019.

[28] H. Karakas, B. Kahraman, İ. Özkol ve M. A. Karabeyoglu, «Hybrid Rocket Nozzle Erosion with Microaluminum-Added Fuel,» *Journal of Propulsion and Power,* 2022.

[29] G. P. Sutton and O. Biblarz, in *Rocket Propulsion Elements*, New Jersey, Wiley, 2010, pp. 53-75.

[30] J. D. Anderson, in *Fundamentals of Aerodynamics*, New York, McGraw-Hill, 2001, pp. 566-575.

[31] M. A. Karabeyoglu, "AA 281a/MECH 427 Advanced Rocket Propulsion Course Notes_Lecture13," Koç University, 2013.

[32] R. H. Stark, "Flow Seperation in Rocket Nozzles, a Simple Criteria," in *41st AIAA/ASME/SAE/ASEE Joint Propulsion Conference & Exhibit*, Tucson, July, 2005.

[33] H. K. Chelliah, A. Makino, I. Kato, N. Araki and C. K. Law, "Modeling of Graphite Oxidation in Stagnation-Point Flow Field Using Detailed Homogeneous

and Semiglobal Heterogeneous Mechanisms with Comparisons to Experiments," *Combustion and Flame,* vol. 104, no. 4, pp. 469-480, 1996.

[34] D. Bradley, Dixon-Lewis G., S. El-din Habik and E. M. Mushi, "The Oxidation of Graphite in Flame Reaction Zones," *Symposium on Combustion,* vol. 20, no. 1, pp. 931-940, 1985.

[35] S. R. Turns, An Introduction to Combustion: Concepts and Applications, 3 ed., Singapore: McGraw-Hill, 2012.

[36] B. R. Bird, W. E. Stewart and E. N. Lightfood, Transport Phenomena, 2 ed., New York: John Wiley & Sons, 2001.

[37] D. R. Bartz, "A Simple Equation for Rapid Estimation of Rocket Nozzle Convective Heat Transfer Coefficients," *Jet Propulsion Laboratory Technical Notes,* vol. 27, no. 1, 1957.

[38] P. Thakre, *Chemical Erosion of Graphite and Refractory Metal Nozzles and Its Mitigation in Solid-Propellant Rocket Motors,* The Pennsylvania State University, Ph.D Dissertation, 2008.

[39] B. J. McBride and S. Gordon, "Computer Program for Calculation of Complex Chemical Equilibrium Compositions and Applications," NASA Reference Publication, Cleveland, 1996.

[40] J. Batchelor ve E. Olcott, «Failure Mechanics in Dense Tungsten Alloy Rocket Nozzles,» *Journal of Spacecraft and Rockets,* cilt 1, no. 6, p. 635, 1964.

[41] P. N. Walsh, J. Ouets, R. Graff ve I. R. Ladd, «Kinetics of the Oxidation of Tungsten bu CO2 at High Temperatures,» *Journal of Chemical Physics,* 1967.

[42] G. R. Belton ve R. L. McCarron, «The Volatilization of Tungsten in the Presence of Water Vapor,» *Journal of Physicsal Chemistry,* cilt 68, no. 7, pp. 1852-1856, 1964.

[43] M. Kalipatrick and S. K. Lott, "Reaction of Flowing Steam with Refractory Metals III. Tungsten," *Journal of Electrochemical Society,* vol. 113, no. 1, pp. 17-18, 1966a.

[44] G. A. Greene and C. C. Finfork, "Vaporization of Tungsten in Flowing Steam at High Temperatures," *Experimental Thermal and Fluid Science,* vol. 25, pp. 87-99, 2001.

[45] C. Unal, W. R. Bohl and K. O. Pasamehmetoglu, "Modeling of Heat and Mass Transfer in Accelerator Targets during Postulated Accidents," *Nuclear Engineering and Design,* vol. 196, pp. 185-200, 2000.

[46] E. A. Gulbransen, K. F. Andrew and F. A. Brassart, "Oxidation of Molybdenum, 550 oC to 1700 oC," *Hournal of Electrochemical Society,* vol. 110, no. 9, pp. 952-959, 1963.

[47] M. Kalipatrick and S. K. Lott, "Reaction of Flowing Steam wit Refractory Metals I. Molybdenum (1100-1700 C)," *Journal of Physical Chemistry,* vol. 69, no. 5, pp. 1638-1640, 1965.

[48] K. A. Weidenmann, G. Rixecker and F. Aldinger, "Liquid Phase Sintered Silicon Carbide (LPS-SiC) Ceramics Having Remarkably High Oxidation Resistance in Wet Air," *Journal of the European Ceramic Society,* vol. 26, pp. 2453-2457, 2006.

[49] J. Roy, S. Chandra, S. Das and S. Maitra, "Oxidation Behaviour of Silicon Carbide - A Review," *Reviews on Advanced Material Science,* vol. 38, pp. 29-39, 2014.

[50] P. J. Macfarlane and M. E. Zvanut, "Dnagling Bond Defects in SiC: the Dependence on Oxidation Time," *Microelectric Engineering ,* vol. 48, pp. 269-272, 1999.

[51] G. V. R. RAO, «Exhaust Nozzle Contour for Optimum Thrust,» 1958.

[52] B. Evans, *Nozzle Erosion Characterization and Minimization for High-Pressure Rocket Motor Applications,* Pennsylvania State University Ph.D Dissertation, August 2010.

[53] R. M. German, "Thermodynamics of Sintering," in *Sintering of Advanced Materials*, WoodHead Publishing, 2010, pp. 3-32.

[54] E. Wheat, M. Vlasea, J. Hinebaugh and C. Metcalfe, "Sinter Structure Analysis of Titanium Structures Fabricated via Binder Jetting Additive Manufacturing," *Journal of Materials & Design,* vol. 156, pp. 167-183, 2018.

[55] H.-M. Kim and Y.-W. Kim, "Low Temperature Pressureless Sintering of Silicon Carbide Ceramics with Alumina-Yttria-Magnesia-Calcia," *Journal of the Ceramic Society of Japan,* vol. 127, no. 4, pp. 207-214, 2019.

[56] K. Raju and D.-H. Yoon, "Sintering additives for SiC Based on the Reactivity: A review," *Ceramics International,* vol. 42, no. 16, pp. 17947-17962, 2016.

[57] E. Gomez, J. Echeberria, I. Iturriza and F. Castro, "Liquid Phase Sintering of SiC wit Additions of Y2O3, Al2O3 and SiO3," *Journal of the European Cerqamic Society 24,* vol. 24, no. 9, pp. 2895-2903, 2004.

[58] A. Malinge, A. Coupe, Y. L. Petitcorps and R. Pailler, "Pressureless Sintering of Beta Silicon Carbide Nanoparticles," *Journal of the European Ceramic Society,* vol. 32, pp. 4393-4400, 2012.

[59] L. Kamps, Y. Saito, R. Kawabata, Y. Takahashi and H. Nagata, "Methof for Determining Nozzle Throat History in Hybrid Rockets," in *52nd AIAA/SAE/ASEE Joint Propulsion Conference*, Salt Lake City, 2016.

[60] R. D'Elia, G. Bernhart, J. Hijlkema and T. Cutard, "Experimental Analysis of SiC-based Refractory Concrete in Hybrid Rocket Nozzles," *Acta Astronautica,* vol. 126, pp. 168-177, 2016.

[61] [C. Soto, C. Garcia-Rosales and J. Echeberria, "Production of Porous SiC by Liquid Phase Sintering Using Graphite as Sacrificial Phase: Influence of SiO2 and Graphite on the Sintering Mechanisms," *Journal of the European Ceramic Society,* vol. 39, pp. 3949-3958, 2019.